Master of Science

Roles of Oxygen Vacancies over $Ni/Ce_xZr_{1-x}O_2$ Catalysts for Ethanol Steam Reforming

The Graduate School of the University of Ulsan

Department of Chemical Engineering

Sang Yoon Kim

Roles of Oxygen Vacancies over $Ni/Ce_xZr_{1-x}O_2$ Catalysts for Ethanol Steam Reforming

Supervisor: Professor Eun Woo Shin

A Dissertation

Submitted to
The Graduate School of the University of Ulsan
In partial Fulfillment of the Requirements for the Degree of

Master of Science

by

Sang Yoon Kim

Department of Chemical Engineering
University of Ulsan
Ulsan, South Korea
January 2022

Roles of Oxygen Vacancies

over Ni/$Ce_xZr_{1-x}O_2$ Catalysts for Ethanol Steam Reforming

This certifies that the master's thesis of Sang Yoon Kim is approved.

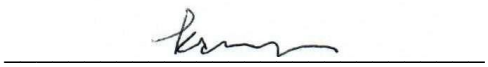

Committee Chair Prof. Sung Gu Kang

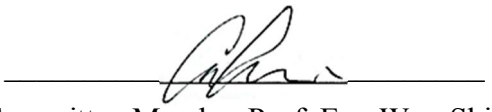

Committee Member Prof. Eun Woo Shin

Committee Member Prof. Jin Suk Chung

Department of Chemical Engineering

University of Ulsan

Ulsan, South Korea

January 2022

ACKNOWLEDGEMENTS

I would like to express my deepest gratitude to my advisor, Professor Eun Woo Shin who has been an invaluable mentor. His gift for firm guidance and enduring encouragement has been an inestimable source of support for me during this process.

I would like to extend my sincere thanks to my committee, Professor Jin Suk Chung and Professor Sung Gu Kang for spending their precious time reviewing this dissertation and supporting this work.

I also had the great pleasure of working with my seniors and present lab mates, Dr. Nguyen Phu Huy, Dr. Do Thi Lien, Dr. Azam Jamsaz, Ms. Nguyen Thi Kim Anh, Ms. Mingyan Wang, Mr. Hae Won Jung, Mr. Dao Duc Quang, Mr. Nguyen Phuong Anh, and Ms. Nguyen Thi Van Anh. Their diverse perspectives and assistance have been of great help to my research. Besides, I would like to express my gratitude to Mrs. Kyoung Jo Lim for her warm and unwavering support and all my friends who were willing to help me.

Finally, the completion of this dissertation would not have been possible without the support and encouragement from my beloved family.

ABSTRACT

The active sites over Ni/$Ce_xZr_{1-x}O_2$ were studied for ethanol steam reforming (ESR). Oxygen vacancy is an essential active site affecting hydrogen production. In this study, to understand catalytic behavior depends on the lattice structures and temperatures over oxygen vacant sites, $Ce_xZr_{1-x}O_2$ as the support was modified with Ce-rich (CZ) and Zr-rich (ZC). Two types of $Ce_xZr_{1-x}O_2$ solid solution were used as support for preparing Ni/CZ (CZN) and Ni/ZC (ZCN) catalysts. ESR for all the catalysts was conducted at 550 and 750 . The CZ catalyst contained higher oxygen vacancy not only on the surface but also in the bulk structure than the ZC catalyst. Ni contributes to the activity of the surface oxygen vacancy of both CZ and ZC catalysts by helping the reduction of the support. The oxygen vacancy in the bulk ZC structure completely disappeared due to the Ni impregnation whereas the bulk oxygen vacancy of CZ was still maintained.

Oxygen vacancy generated active oxygen species via the steam activation and then, the active oxygen species simultaneously involved steam reforming, water gas shift reaction, and ethylene oxidation during ESR. From the reaction result, the lack of oxygen vacancy over ZC resulted in limited reaction routes due to limited active oxygen species. The ZC catalyst, when compared with CZ, exhibited the limitation of the ethylene oxidation at 550 and water gas shift reaction at 750 , respectively. With the Ni species, even though the surface oxygen vacancy behavior over CZN and ZCN was the same, the oxygen-involved reaction was enhanced with the bulk oxygen vacancy of CZN, resulting in the highest H_2 production of 1112.2 μmol/g•min for the CZN catalyst.

TABLE OF CONTENTS

LIST OF FIGURES

LIST OF TABLES

NOMENCLATURES

Abbreviations

BET	Brunauer Emmett Teller
TOS	Time on Stream
XPS	X-ray Photoelectron Spectroscopy
XRD	X-ray Diffraction

Roman and Greek letters

E_g	Optical and gap energy (eV)
d	Average crystallite size (nm)
S_{BET}	Specific surface area (m^2/g)
λ	Wavelength (nm)

Chapter 1: Introduction

1.1 Global energy demand increases and hydrogen energy as an alternative

Fossil energy has been a primary energy source of the technological, social, economic and development progress which has followed. This has continued in the beginning of the 21st century with almost all energy from gasoline, diesel, or natural gas. The continued use of fossil fuels to meet most of the world's energy demand is threatened by rising concentrations of carbon dioxide (CO2) in the atmosphere and concerns about global warming [1].

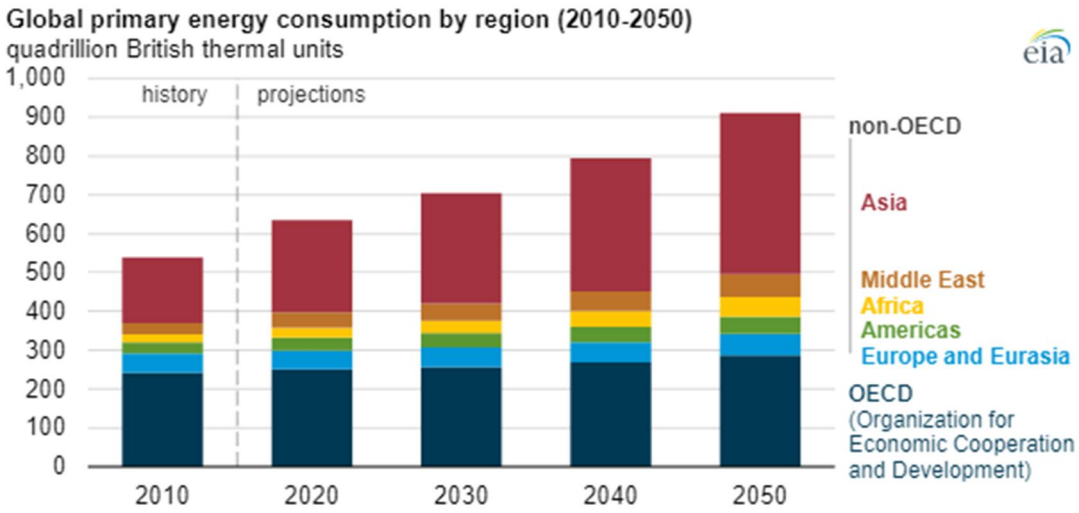

Figure 1.1. Global primary energy consumption by region (2010-2050) [2]

Fossil fuels depletion and rising concerns on the global warming issue resulted from fossil fuel burning causing CO_2 emission as shown in Fig. 1.2, and it necessitates the development and utilization of sustainable alternative energy resources. The sustainability of industry and economy with high renewable energy source rates is a topic of major interest, especially when considering the intermittency of renewable energy source (RES) production and the actual growing trend of energy consumption [2]. The transition from fossil fuels to RESs is the inevitable choice Before major disruptions caused by fossil fuel-based energy supply and environmental issues.

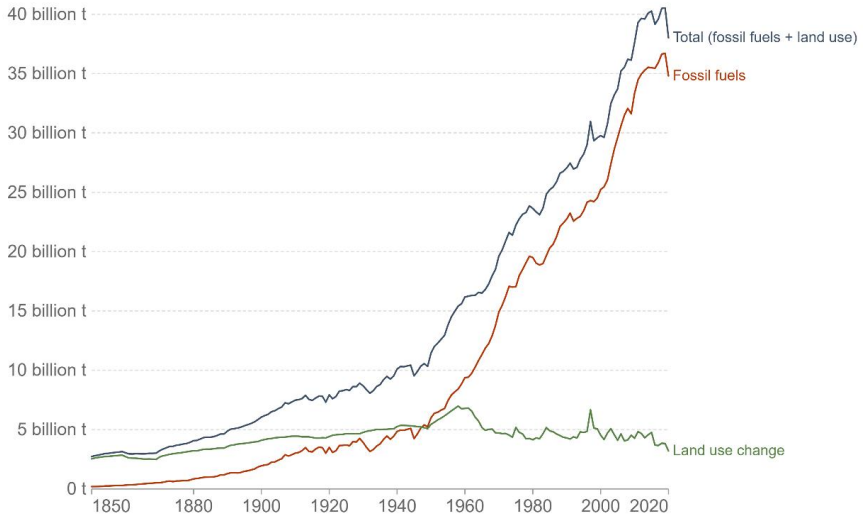

Figure 1.2. Global CO emissions from land-use change [3]

Among the renewable energy sources investigated, hydrogen (H_2) is likely of utmost importance as highly feasible energy due to its highest energy content per weight (120 MJ/kg) and environmental beingness [4]. Today, H_2 is widely used in electronics, fuel cells, refinery, metallurgical-processing industries, etc. [5]. The application of H_2 in internal combustion engines and fuel cells also gained substantial significance, credited to its clean emission (no carbon dioxide, CO2 is emitted) [6]. As shown in Fig. 1.3, most of the H_2 is generated from fossil fuels (coal and natural gas), with approximately 50% of H_2 production coming from the steam reforming (SR) of natural gas and other light hydrocarbons [7].

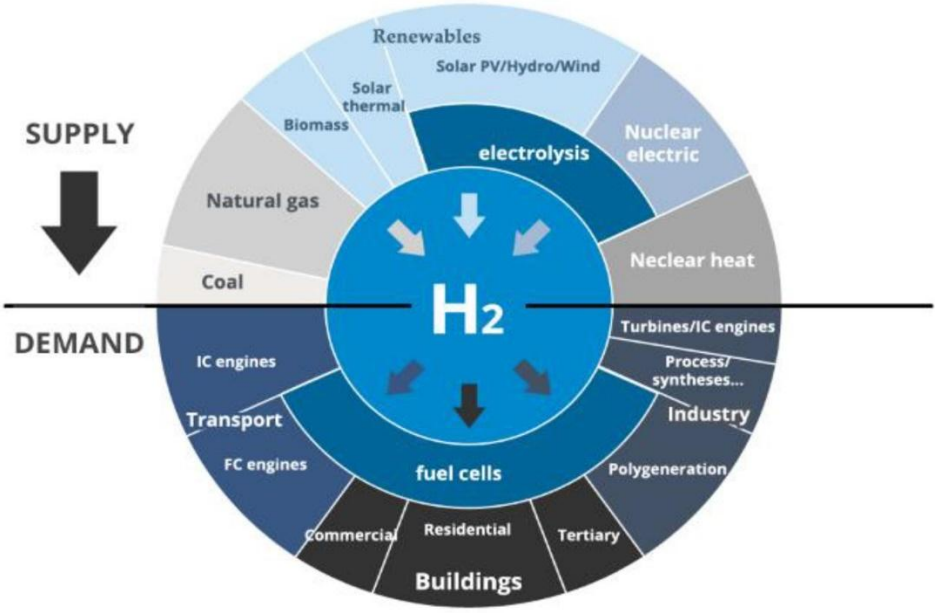

Figure 1.3. Primary sources of H_2 and its application [8]

1.2 H_2 production using ethanol(C_2H_5OH) steam reforming technology.

Recently, as global interest in the environment has increased, interest in hydrogen (H_2) as clean energy is growing rather than fossil fuels such as petroleum and coal [6, 7]. However, the natural gas reforming reaction and coal gasification processes using hydrocarbons as fuel for hydrogen production inevitably emit greenhouse gases during the reforming process. Therefore, there is a growing demand for an environmentally friendly hydrogen production process that is different from the existing hydrogen production processes. Accordingly, the ethanol steam reforming reaction is receiving great attention as an environmentally friendly clean hydrogen production process that can realize carbon neutrality. Ethanol is non-toxic, and when bioethanol produced mainly through fermentation of saccharide [9, 10] is used as feed, carbon neutrality can also be achieved because carbon dioxide generated from reforming can be reabsorbed into biomass as a raw material.

Steam reforming of C_2H_5OH is reversible and not simple to maintain. On the other hand, complete C_2H_5OH conversion is essential for the process to be economical. The catalyst has an important role in achieving this because it increases the rate of reaction in such a way that the system tends toward thermodynamic equilibrium [11]. However,

different catalysts induce different pathways to produce H_2. Therefore, the development of suitable catalysts has a vital role in the reforming process [12].

Nickel-based catalysts are investigated for this process, leading to high hydrogen yield at the high reaction temperature, due to their C–C bond cleavage ability [13, 14]. Usually, these catalysts are dispersed in a matrix formed by pure or mixed oxides like Al_2O_3 [15] with CeO_2–ZrO_2 solid solutions as co-catalyst [16, 17]. Ni-based catalysts have a strong tendency to sintering and to form coke in reforming reactions. The nature of the support like Al_2O_3 has also great importance for the catalytic performance of supported metals as catalysts for ethanol steam reforming reaction. From a practical point of view high surface area Al_2O_3, which provides good mechanical properties and relatively low cost is widely used as support to maximize the exposed surface of the metal. The use of second metal can give rise to different structures like alloys which are more resistant to carbon deposition due to decreased solubility and diffusion of carbon atoms in metal nanoparticles [18, 19]. The other oxides, such ZrO_2, CeO_2–ZrO_2 solid solutions ($Ce_xZr_{1-x}O_2$), ZnO, and La_2O_2, have been also widely used [16, 17]. As an important rare-earth oxide material, ceria is widely applied in industry forming a solid solution with zirconia. The oxygen storage capacity (OSC) and the metal-support interaction in oxygen-buffer ceria-zirconia based metal catalysts always showed higher catalytic activity when compared with non-oxygen-buffer oxides [20, 21]. It stores oxygen by filling oxygen vacancies in the oxygen storage material (OSM). Maximizes oxygen storage capacity through large deviations of the oxygen specific non-stoichiometry δ, for example $CeO_{2-\delta}$ [22]. Through the reduction/oxidation of Ce^{4+} (Zr^{4+}) and Ce^{3+} (Zr^{3+}), $CeO_{2-\delta}$ and $ZrO_{2-\delta}$ can release and incorporate oxygen [22].

1.3 Research objectives

It is well known that $Ce_xZr_{1-x}O_2$ solid solutions have a high oxygen storage capacity with oxygen vacancy which plays the important role of enhancing catalytic activity under reducing and oxidizing conditions [23]. Therefore, tracking the reaction pathway of oxygen vacancy is very important for the elucidation of the mechanism of ethanol steam reforming. However, there are several reaction pathways (Fig. 1.4) that could occur in the ethanol steam reforming process [24]. The complex mechanism, which is a disadvantage of ethanol steam reforming, greatly hinders the tracking of the reaction pathway.

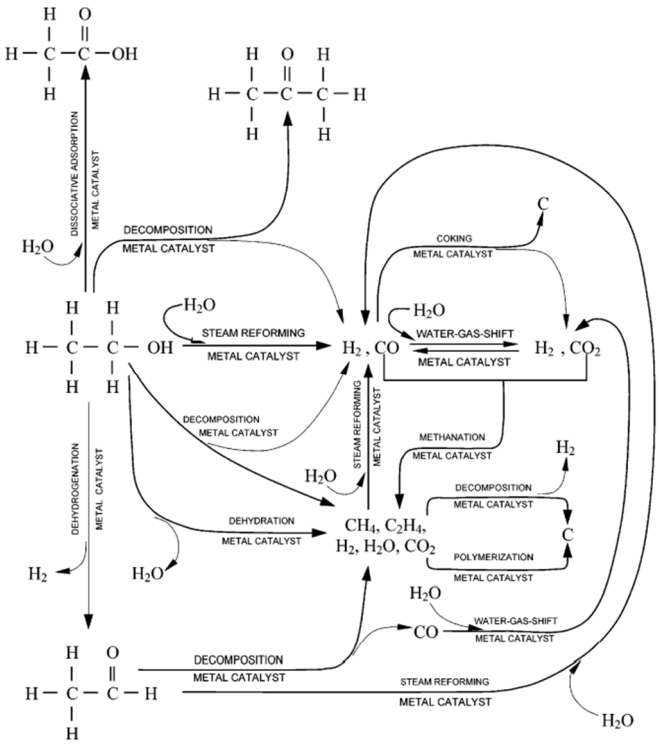

Figure 1.4. Reaction pathways that can occur during ethanol steam reforming over metal catalysts [12]

To clarify the mechanism, the catalyst configuration was simplified by excluding alumina. Although Al_2O_3 support exhibits high surface area and high activity in the reforming process, they can easily undergo deactivation due to the formation and subsequent accumulation of carbon deposits [15]. It occurs due to various side reactions such as Boudouard reaction (Eq. 1), decomposition of methane (Eq. 2).

Boudouard reaction

$$2CO \rightarrow CO2 + C \qquad \Delta H_r^{o}{}_{298} = -\ 172 kJ/mol \qquad (1)$$

Decomposition of methane

$$CH_4 \rightarrow 2H_2 + C \qquad \Delta H_r^{o}{}_{298} = 75 kJ/mol \qquad (2)$$

Moreover, the catalytic performance of gas-phase reactions over the ceria-zirconia based catalysts was found significantly influenced by structures, which were originated from the different arrangements of atoms in different crystal planes that resulted in different specific surface energies, metal dispersion, and metal-support interaction [25-28].

However, to our knowledge, there has been no report on the role of oxygen vacant sites over Ni/$Ce_xZr_{1-x}O_2$ in ESR depending on structure and temperature. In hence, $Ce_xZr_{1-x}O_2$ catalysts with two major different phase structures were prepared with a specific ratio of Ce/Zr as a support (Fig. 1.5). Ni/$Ce_xZr_{1-x}O_2$ catalysts were prepared by impregnating Ni species into the cubic and tetragonal $Ce_xZr_{1-x}O_2$ supports to investigate not only the formation of oxygen vacancy by Ni-$Ce_xZr_{1-x}O_2$ interaction but also the role of oxygen vacancy in the reaction pathways of ESR.

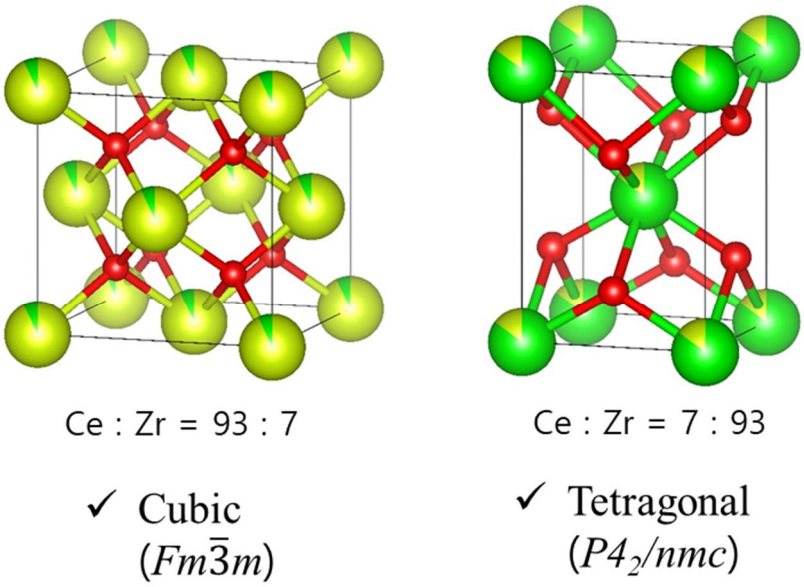

Figure 1.5. Phase structure of Ce-rich catalyst and Zr-rich catalyst

Chapter 2: Experiments

2.1 Catalyst preparation

Two kinds of $Ce_xZr_{1-x}O_2$ supports with different Ce/Zr ratios were prepared by use of the sol-gel method, using an aqueous solution of $Ce(NO_3)_3 \cdot 6H_2O$ (≥99%; Sigma-Aldrich Korea, Gyeonggi, South Korea) and $ZrO(NO_3)_2 \cdot xH_2O$ (99%; Sigma-Aldrich Korea, Gyeonggi, South Korea) as precursors [29-31]. Appropriate amounts of cerium nitrate, zirconium nitrate, and citric acid were dissolved in distilled water at a rate of 600 rpm with a magnetic stir bar on a stir plate. The molar ratio of citric acid to metal precursor was 1:2. A transparent solution was heated at 70 during preparation. After obtaining opaque viscous gel while heating, ethylene glycol was added into the continuously agitating dissolved solution. The molar ratio of ethylene glycol to citric acid was 1:2.5. In this method, a metal salt is dissolved in a solution with citric acid and ethylene glycol to form a homogeneous precursor solution containing metal–citrate chelate complexes. A more viscous gel was formed and then decreased the stirring rate to 300 rpm while maintaining the temperature for 10-20 minutes. Then the mixture was dried at 120 °C for obtaining a homogeneous gel. The gel was dried at 120 °C for 3 h and heated under N_2 at 800 °C for 1 h. Then the mixture was calcined at 700 °C for 6 h with a rate of 2 °C/min. Ni impregnated catalysts were synthesized using the wet impregnation method with the rotary evaporator using an aqueous solution of $Ni(NO_3)_2 \cdot 6H_2O$ (Sigma-Aldrich, Gyounggi, South Korea). The amount of Ni in the solution was calculated to be 10 wt.% on each support. After nickel impregnation, these catalysts were dried at 85 °C for 12 h and then, calcined at 700 °C for 4 h with the rate of 1.5 °C/min. Ni-impregnated catalysts were reduced in the hydrogen atmosphere before doing ethanol steam reforming reaction experiments. In all catalysts, the molar ratio of cerium to zirconium is shown in Table 1, and "N" after support means nickel impregnated.

2.2 Catalyst characterization

The Brunauer–Emmett–Teller (BET) surface area of the catalysts was detected by nitrogen adsorption/desorption on an ASAP 2020 apparatus (Micromeritics, Norcross, GA, USA). Crystal sizes were calculated using the Scherrer equation from X-ray diffraction (XRD) patterns on a RAD-3C diffractometer (Rigaku Corp., Tokyo, Japan) with copper K-α radiation (k = 1.5418 Å) at a scan rate of 5º(5θ)/min, operated at 40 kV and 30 mA. The Raman spectra were obtained with a DXR Raman Microscope (Thermo Fisher Scientific, Waltham, MA, USA) using a 532-nm excitation source. X-ray photoelectron spectroscopy (XPS) data were obtained through the use of the Thermo K-alpha XPS with an aluminum K-a X-ray source (Thermo Fisher Scientific, Waltham, MA, USA). The samples were collected using an X-ray spot size of 400 μm, pass energy of 50 eV, and an energy step size of 0.1 eV. Hydrogen temperature-programmed reduction (H2-TPR) was carried out in a multipurpose analytical system (BELCAT-M, MicrotracBEL Corp., Osaka, Japan) using a thermal conductivity detector (TCD). Nitrogen gas and mixture gas (5% H_2 in N_2) was used as a carrier gas and a reducing gas, respectively. The ramp rate was 2 ºC/min from 50 to 900 .

2.3 Reaction test

The overall reaction test is summarized in fig. 2.1. Experiments were performed at atmospheric pressure in a fixed-bed vertical quartz tube reactor of 450mm in length and 10mm i.d. In all experiments, 0.3 g of catalyst was used as it was placed on a frit inside the reactor with glass wool. Catalysts were reduced in situ in flowing H_2 (6 mL/min) with helium (30 ml/min) at 750 for 2 h. The flow rate of each gas was controlled by a mass flow controller. After the reduction step, stop the hydrogen supply and then mixture flow of water and ethanol (0.05 mL/min) and helium flow (70 mL/min) were vaporized at 180 ◦C and fed into the fixed-bed reactor. Water and ethanol mixture (EtOH/H2O = 15:85 mol/mol) were pre-mixed in a separate container and fed to the reactor by a pump (Model SP-22-12S; FLOM, JAPAN). Helium was used as a carrier gas. Then the reaction tests were conducted for 8 h at 550 and 750 . Steam to carbon mole ratios (S/C = 3) was adjusted for every reaction test. Gas product was sampled and analyzed directly every 30 minutes. Liquid products are stored in a connected low-temperature container after the reactor during the reaction and then analyzed. The product stream was analyzed by two

different gas chromatographs. The first chromatography (Acme 6000 GC, YL Instrument Co., Ltd., Dongan-gu, South Korea) for the gas product, equipped with a packed column (Supelco) and a TCD with He as the carrier gas, was used for the analysis of H_2, CO, CH_4, CO_2, C_2H_4. The second chromatography (Agilent 6890 N Network GC, Agilent Technologies, Inc., Santa Clara, CA, USA) for the liquid product, equipped with a capillary column (Agilent) and TCD with Helium as the carrier gas, was used for the analysis of ethanol and acetone.

The ethanol conversion, H_2 selectivity, H_2 production rate, and carbon – containing product selectivity from the reaction results were determined from:

$$Ethanol\ \ conversion\ \ (\%) = \frac{nEtOH_{in} - nEtOH_{out}}{nEtOH_{in}} \times 100,$$

$$H_2\ \ selectivity\ \ (\%) = \frac{nH_2}{nH_2 + 2nCH_4 + 2nC_2H_4},$$

$$H_2\ \ production\ \ rate\ \ (\mu mol/g_{catal.} \cdot min) = \frac{nH_2\ \ per\ \ min}{mass\ \ of\ \ catalysts},$$

and

$$Carbon - containing\ \ product\ \ selectivity = \frac{j \times n_i}{\sum j \times n_i},$$

Where n_i is the moles of the product i, and j represents the number of carbon atoms in the carbon-containing product.

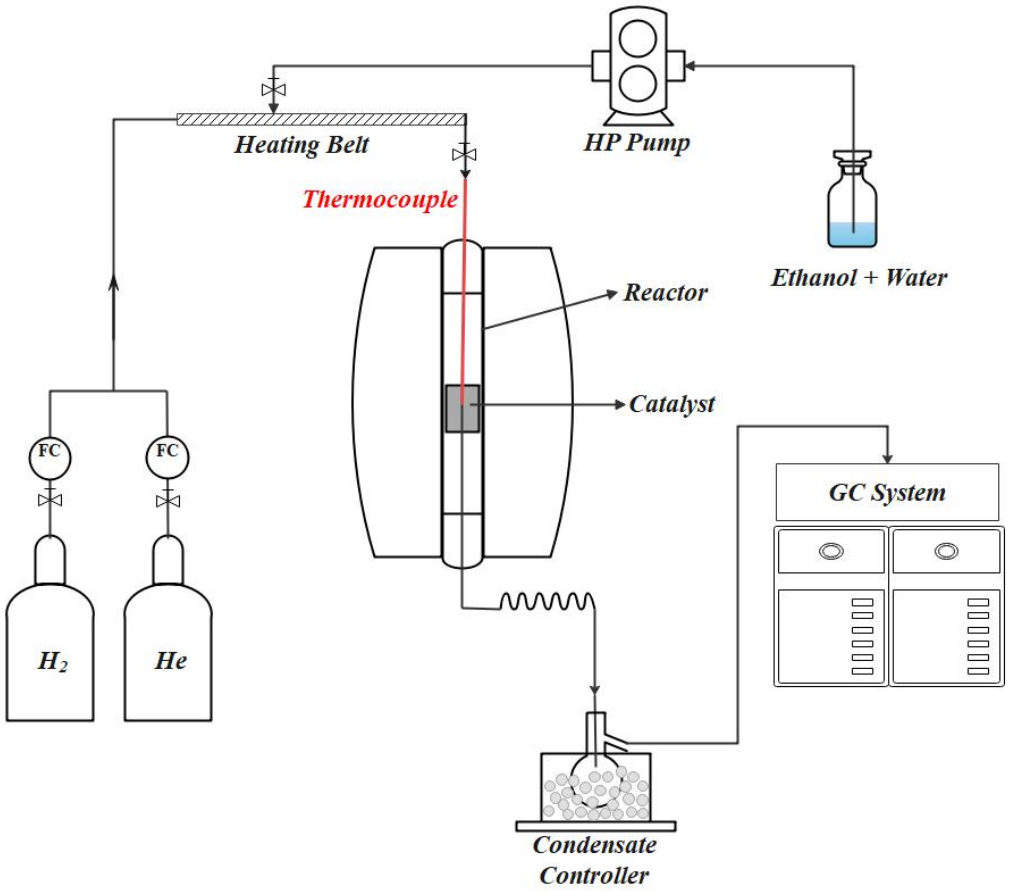

Figure 2.1. Schematic diagram of the ethanol steam reforming reaction system

Chapter 3: Results and discussion

3.1 Catalyst characterizations

3.1.1 BET

Table 1 summarizes BET surface areas for all synthesized samples. Nitrogen adsorption isotherm and Pore-size distribution of $Ce_xZr_{1-x}O_2$ and $Ni/Ce_xZr_{1-x}O_2$ catalysts are summarized in Fig. 3.1 and Fig. 3.2, respectively. The $Ce_xZr_{1-x}O_2$ catalysts showed an IUPAC type IV of isotherms with the hysteresis type H1 [32] and after nickel was impregnated, in the $Ni/Ce_xZr_{1-x}O_2$ catalysts showed an IUPAC type IV of isotherms with the hysteresis type H4 [33]. The BET surface area results were similar to those reported by Liotta [34]. In addition, according to the study of Noelia [35], the surface area of the solid solution of ceria-zirconia varies greatly depending on the calcination temperature, and the results calcinated at 750°C in this study showed a value between 500°C and 1000°C of the above study. From the results, the BET surface areas decreased as Ni loaded. It is probably because Ni is impregnated in the pores on the support, as it can be seen that the existing pore volume is decreased in Fig. 3.2.

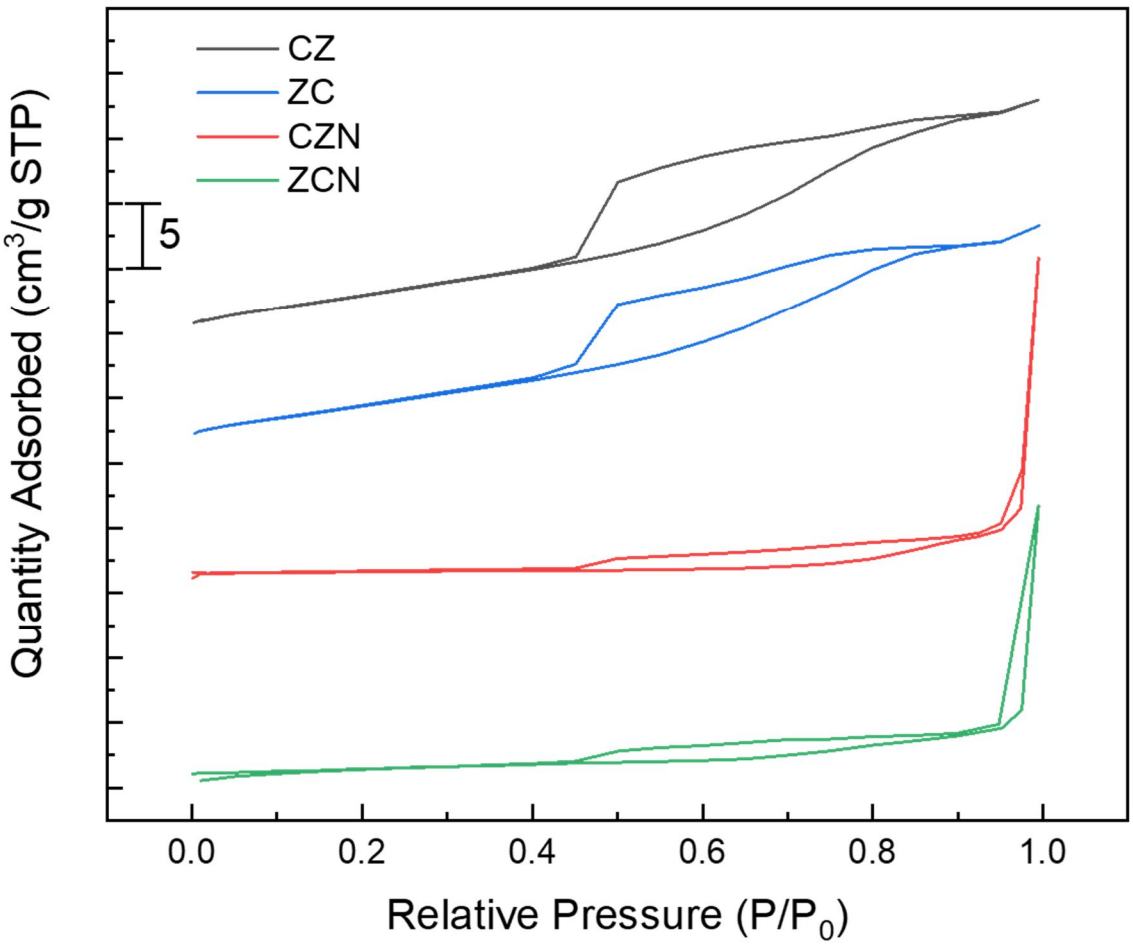

Figure 3.1. N2 adsorption-desorption isotherms of Ni/$Ce_xZr_{1-x}O_2$ and $Ce_xZr_{1-x}O_2$ catalysts

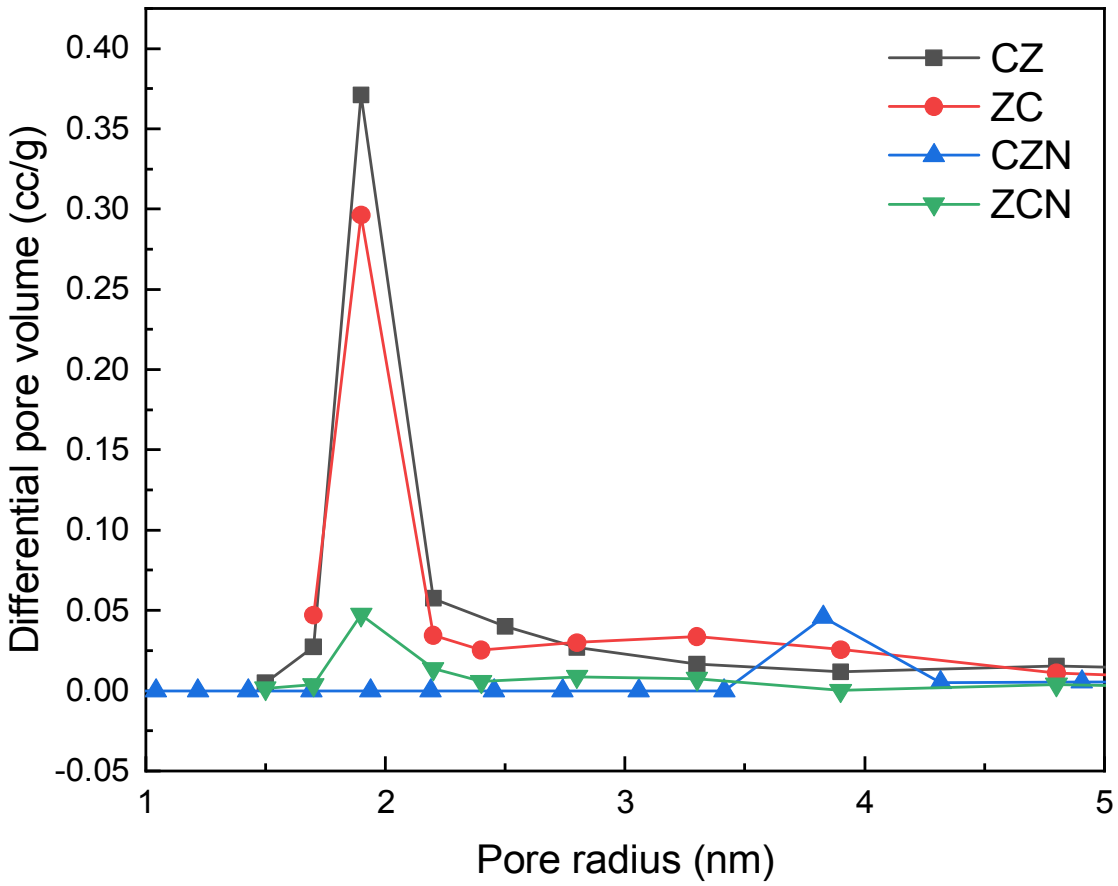

Figure 3.2. Pore-size distribution of Ni/$Ce_xZr_{1-x}O_2$ and $Ce_xZr_{1-x}O_2$ catalysts

Table 1. Structural parameters and surface area of $Ni/Ce_xZr_{1-x}O_2$ and $Ce_xZr_{1-x}O_2$ catalysts

Catalyst	S_{BET} (m^2/g)	Ce/Zr ratio		Ni contents (%)	Ni particle size* (nm)	(111) support particle size* (nm)
		Theoretical	XRD			
CZ	19.0	93/7	91/9	–	–	13.2
CZN	15.4	93/7	90/10	10.0	59.9	14.7
ZC	6.4	7/93	90/10	–	–	13.0
ZCN	3.1	7/93	85/15	10.0	50.3	13.8

** The values are calculated from the Scherrer equation.*

3.1.2 XRD

The crystalline structures of the Ce-rich and Zr-rich catalysts are shown in Fig. 3.3. CZ sample showed visible peaks at 2θ = 28.59°, 33.15°, 47.59°, and 56.49° which represent the indices of (111), (200), (220) and (311) planes, respectively. ZC sample showed visible peaks at 2θ = 30.07°, 34.55°, 35.06°, 58.99°, and 59.89° which represent the indices of (101), (002), (110), (112) and (200) planes, respectively. The $Ce_xZr_{1-x}O_2$ peak positions of each plane provided evidence of the homogeneity and actual composition of a solid solution. In addition, XRD results showed that the Ce-rich and Zr-rich catalysts possessed the characteristic peaks of cubic (ICDD, 01-075-9469, Fm3m (225)) and tetragonal (ICDD, 01-074-8058, $P4_2/nmc$ (137)) structures.

The XRD figure was plotted with three lines, each line showing a different stage of the catalyst. This was to observe the different behaviors due to the different interactions of Ni and support in each step. Each row means after reduction, after calcination, and in a support state before the Ni impregnated. Nickel oxide (ICDD, 00-047-1049, Fm3m (225)) and Nickel (ICDD, 00-004-0850, Fm3m (225)) peaks were evident after calcination and after reduction, respectively. In addition, the Ni crystallite sizes and Ce and Zr solid solutions crystallite sizes were calculated using the Scherrer equation corresponding to the Ni (1 1 1) peak in the "After reduction" XRD patterns, and the results are summarized in Table 1.

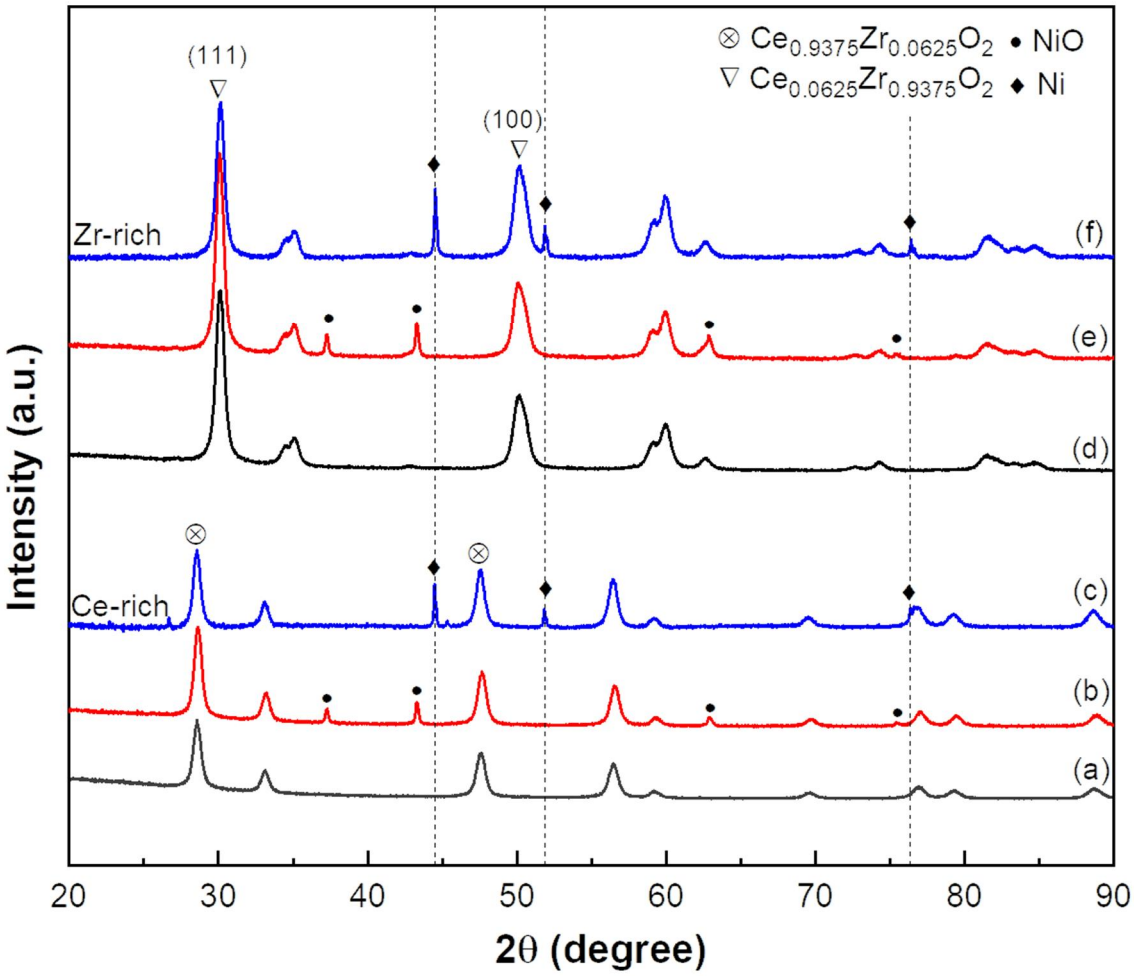

Figure 3.3. XRD patterns of Ce-rich and Zr-rich catalysts obtained from 3 steps: Support ((a), (d)), After calcination ((b), (e)), and After reduction ((c), (f)).

3.1.3 Raman spectroscopy

Raman spectroscopy is a very useful method in characterizing the structure of the support, and it also can be employed for the change in the structure after impregnation of Ni through observing stress-induced Raman band shifts [36]. Fig. 3.4 shows the Raman spectra of the CZN, CZ, ZCN, and ZC.

F_2g mode detected on the CZ graph at 469 cm^{-1} is characteristic of cubic fluorite ceria oxides and is attributed to the symmetric stretching of oxygen around cerium cations in the CeO_8 vibrational [37]. The spectrum of ZC revealed that a tetragonal structure was formed on ZC catalyst, as evidenced by the set of characteristic bands at 146, 260, 316, 460, 600, and 641 cm^{-1} [38]. In addition, the state of the main peak of support was shown in the graph in order as Ni is impregnated. Among the various peaks, the main peak of CZ was the Ce-O-Ce peak (F_2g) located at 469 cm^{-1}, and the main peak of ZC was the Zr-O-Zr peak (Eg) located at 260 cm^{-1}.

The shift in the main characteristic Raman peak is due to the incorporation of Ni, which changes the bonding between atoms because of differences in size [39]. The total difference between before and after loading of Ni was 14-15 cm^{-1} on both CZN and ZCN. However, the difference between each step was a more remarkable result. The graph "after calcination" indicated that Ni was impregnated in the NiO state and the graph "after reduction" indicated that it was impregnated in the Ni state. In the case of CZN, a shift occurred by 13 cm^{-1} from 469 to 456 cm^{-1} when NiO was impregnated, and the peak shifted by 2 cm^{-1} from 456 to 454 cm^{-1} when NiO was then reduced to Ni. On the other hand, in the case of ZCN, the peak shifted by 14 cm^{-1} from 260 to 246 cm^{-1} only when Ni was reduced. These results indicate that CZN has strong metal-support interaction, which causes Ni to be impregnated more deeply as well as with less energy.

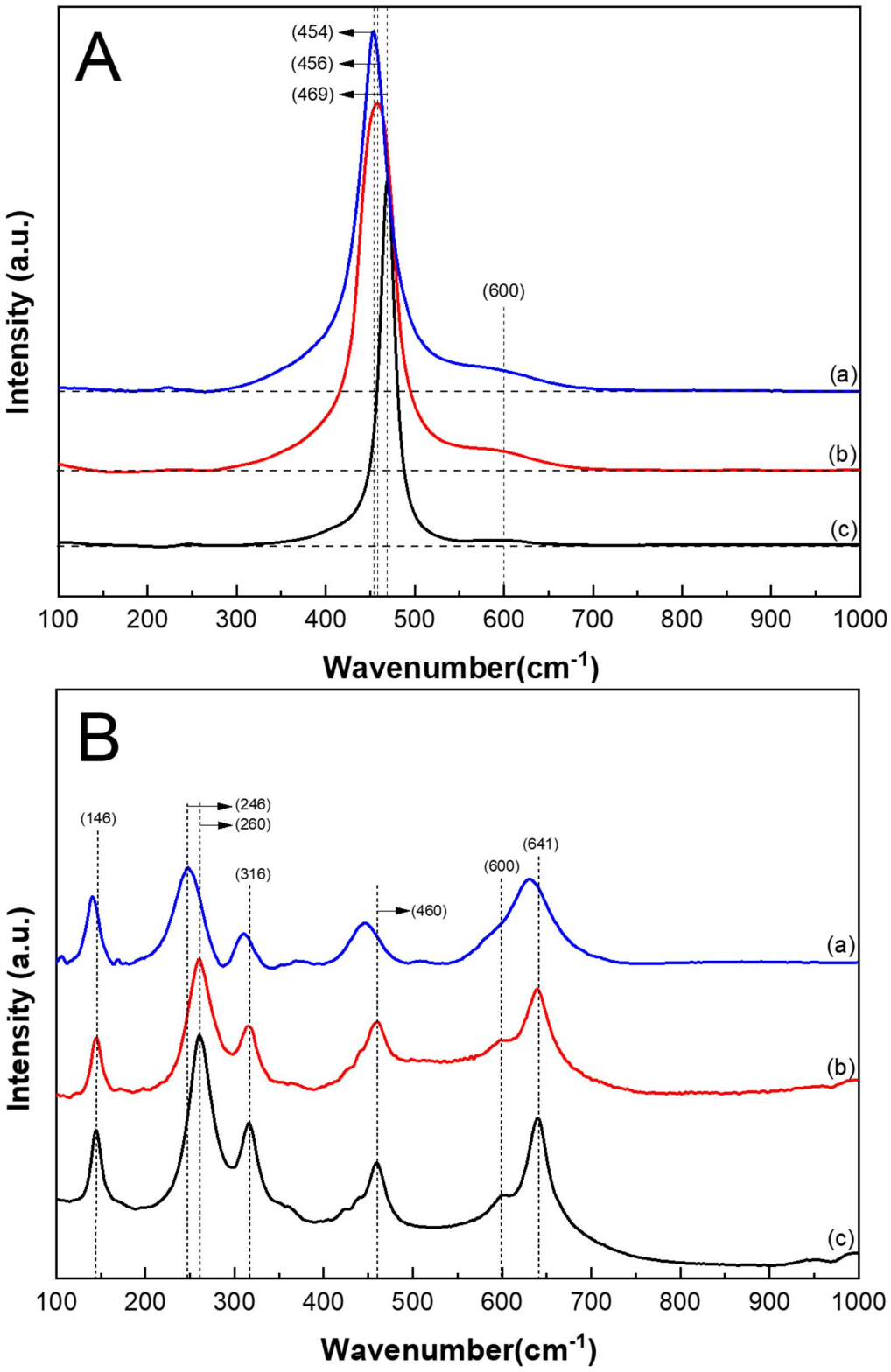

Figure 3.4. Raman spectra of (A) Ce-rich and (B) Zr-rich catalysts obtained from 3 steps: (a) After reduction (CZN and ZCN), (b) After calcination, and (c) support (CZ and ZC).

3.1.4 H_2-TPR

H_2-TPR is usually performed to characterize the redox properties of materials. The corresponding profiles using H_2-TPR of all supports and Ni impregnated catalysts are shown in Fig. 3.5.

Two main reduction peaks were noted for both CZ and ZC support, one between 450 and 550 , representing surface reduction, and the other around 736 representing bulk reduction [37]. The hydrogen consumption for the reduction in the surface, bulk, and nickel oxide on the $Ce_xZr_{1-x}O_2$ support is shown in Table 2. TPR profiles are very important to prove oxygen vacancy on each catalyst. In this study, all the supports were reduced in-situ at 750 °C, implying that the formation of Ce^{3+} and Zr^{3+} on supports occurred on the surface and bulk [40]. And that oxygen-deficient generated the oxygen vacancy. Therefore, total hydrogen consumption from the reduction peak can be considered as the amount of oxygen vacancy, and CZ (0.166 mmol/g) shows 2.4 times larger than that of ZC (0.070 mmol/g).

When nickel was impregnated, the peak tendency was changed. First, a large reduction peak occurred in the low-temperature portion. In the enlarged TPR profiles of Ni-impregnated catalysts (Fig. 3.6), two NiO reduction ranges were observed. The first one was a reduction of NiO interacting weakly with the support (300 °C–350 °C) and the second one, which appears only in CZN, was a reduction of NiO interacting strongly with a $Ce_xZr_{1-x}O_2$ support (350 °C–380 °C).

Second, the shift to the lower temperature of the surface oxygen peak. When Ni was impregnated, hydrogen spilled over from the metal helps the reduction of the support, and surface oxygen vacancy sites were formed more easily [41]. As a result, the peak of the support shifted to a lower temperature. And the formation similar amount of surface oxygen vacancy was 0.083 and 0.076 mmol/g in CZN and ZCN, respectively.

Third, the bulk reduction part of the support around 736 °C. In CZN, the bulk peak was maintained similarly, but in ZCN, the bulk peak disappeared. The formation amount of bulk oxygen vacancy was 0.086 mmol/g in CZN only. These results indicated a change in bulk oxygen vacancy, and there was no formation of bulk oxygen vacancy in ZCN. When connecting the NiO (350 °C–380 °C) and the bulk results, the influence of Ni in the lattice structure was different, and ZCN had a structure that prevents the formation of

oxygen vacancy. Schematic of the oxygen vacancy behavior of all catalysts based on the H_2-TPR results is summarized in Fig. 3.7.

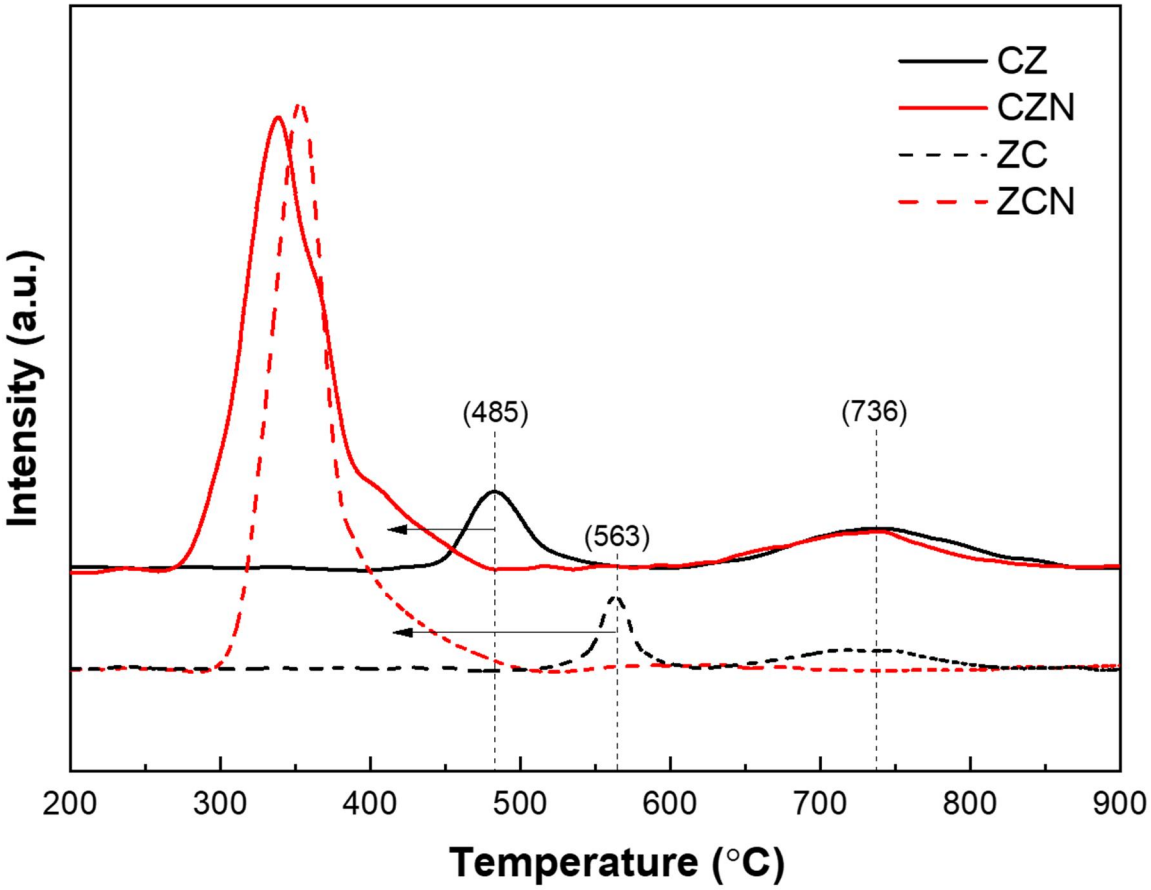

Figure 3.5. H_2-TPR profiles of CZ, CZN, ZC, and ZCN

Table 2. Quantitative analyses of surface oxygen species-derived H_2 consumptions in H_2-TPR.

Catalyst	H_2 consumption (mmol/$g_{catal.}$)		
	Surface Ov	**Bulk Ov**	Total
CZ	0.075	0.091	0.166
CZN	0.083	0.084	0.169
ZC	0.044	0.026	0.070
ZCN	0.076	0	0.076

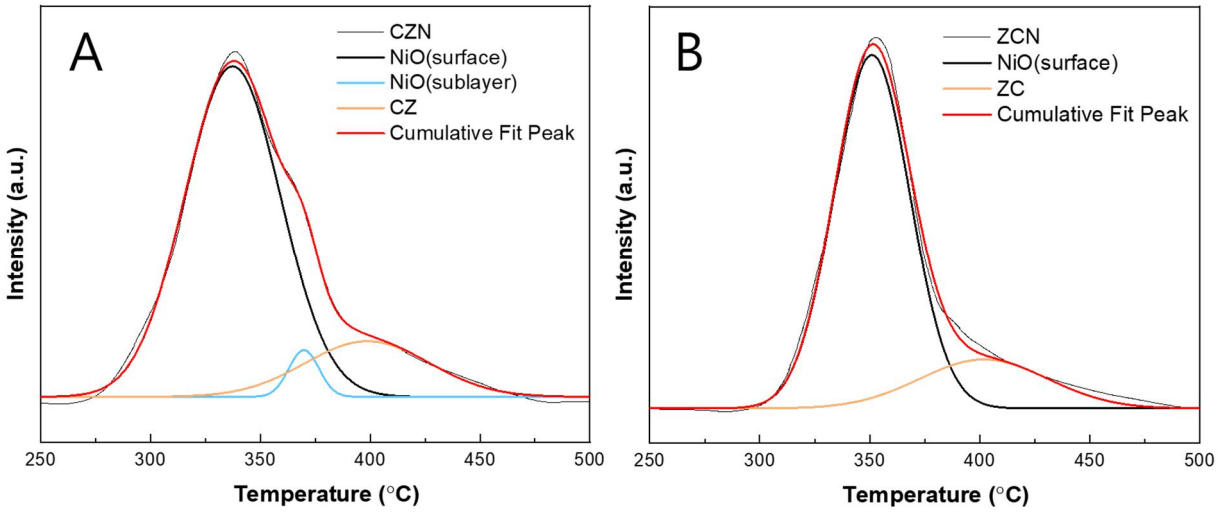

Figure 3.6. H_2-TPR profiles of (A) CZN (B) ZCN catalysts with peaks assigned in the temperature range of 250 □ to 500 □.

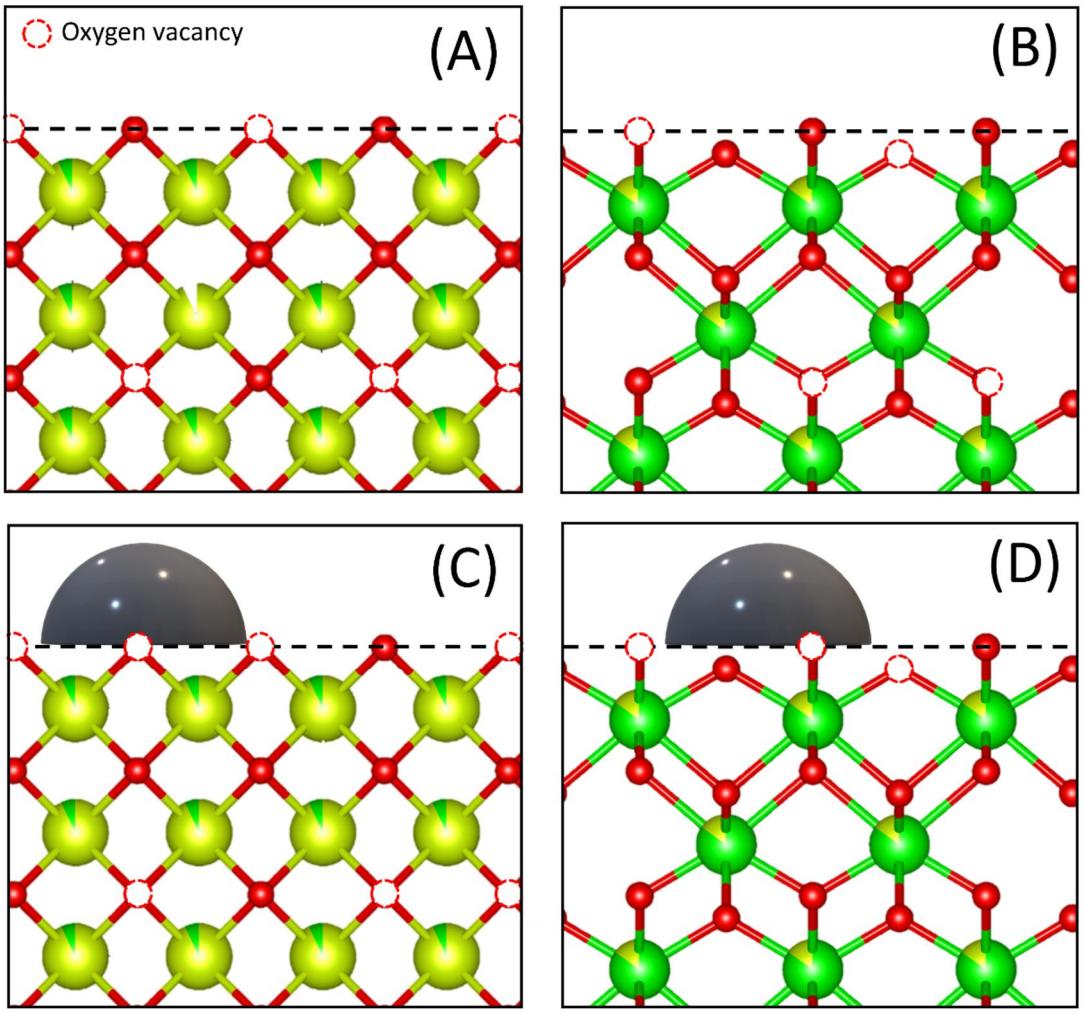

Figure 3.7. Schematic of oxygen vacancy on (A)CZ, (B)ZC, (C)CZN, and (D)ZCN.

3.1.5 XPS

XPS was performed to confirm the electronic state of Me^{3+} (Me = Ce or Zr) that creates oxygen vacancy and the Ni metallic site impregnated on the surface. The XPS data of Ce 3d, Zr 3d, and Ni 2p of the support and Ni impregnated catalysts are shown in Fig. 3.8. In the Ce 3d spectra (Fig. 3.8 – (A)), which showed the characteristics of Ce-rich catalysts, the peaks marked as v, v_2, v_3, u, u_2, and u_3 corresponded to Ce^{4+} species, while the peaks denoted by v_1 (884.1 eV) and u_1 (902.4 eV) were assigned to Ce^{3+} with oxygen vacancies [42-44]. In the Zr 3d spectra (Fig. 3.8 – (B)), which shows the characteristics of Zr-rich catalysts, two broad peaks related to Zr $3d_{5/2}$ and Zr $3d_{3/2}$ were observed. The curves of the Zr-rich catalysts were fitted to Zr^{3+} and Zr^{4+} species, with Zr $3d_{5/2}$ 184.2 eV and 182.0 eV, respectively, with a spin-orbit splitting value of 2.6 eV [45, 46]. An increase in the M^{3+} (M = Ce or Zr) peak area indicated an increase in oxygen vacancy, and the change was confirmed in the support, calcination, and reduction stages. For CZN, it increased to 7.0, 7.1, and 9.1%, respectively, and for ZCN, it increased to 21.6, 23.4, and 44.0%, respectively. As Ni was impregnated, oxygen vacancy increased with hydrogen spillover from Ni, which is in agreement with the results of H_2-TPR.

The Ni 2p XPS data (Fig. 3.8 – (C)) can be assigned into four peaks which consist of three peaks and one satellite peak. The first peak at 855.5eV and two smaller peaks at 854.0 and 852.5eV were assigned to Ni^{3+} form of Ni cluster [47], Ni^{2+} of Nickel oxide (NiO) [48, 49] and Ni^{+} of metallic nickel (Ni) [49], respectively. Ni was impregnated on the catalyst in the form of NiO in the calcination step. And in the reduction step, NiO was reduced to Ni as the Ni peak appears in the graph. From the Ni-2p XPS results, the area of the Ni peak was much smaller in CZN than in ZCN. Because XPS analyzes the surface at about 10nm, it is difficult to observe Ni impregnated on the bulk. However, in the case of ZCN, most of the Ni was located on the surface, and the peak of the Ni metallic site appeared large, which prevented the desorption of oxygen from the bulk. This indicated that the formation of the bulk oxygen vacancy was disturbed, and it was the same as the results of Raman spectroscopy and H_2-TPR.

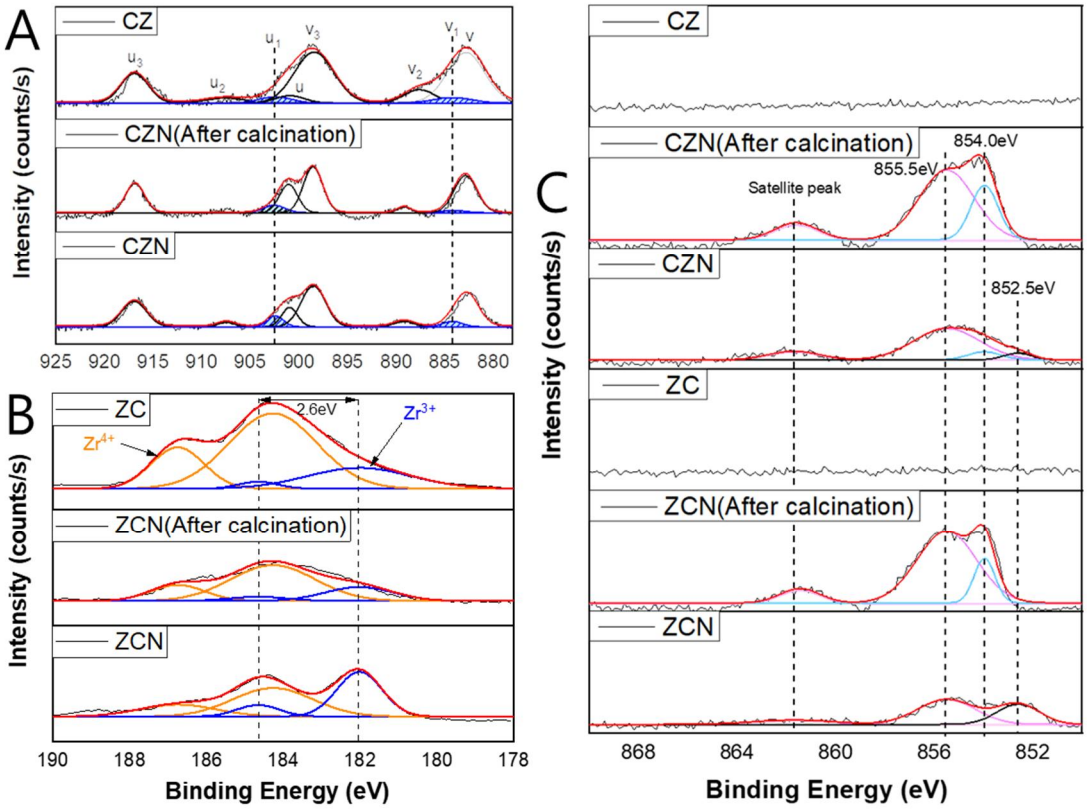

Figure 3.8. XPS (A) Ce 3d, (B) Zr-3d, and (C) Zr 2p of Ce-rich and Zr-rich catalysts obtained from 3 steps: After reduction (CZN and ZCN), After calcination, and support (CZ and ZC).

Table 3. The binding energy of O 1s and Ni 2p lines and the corresponding surface atomic concentration of catalysts.

XPS	Peak	Peak intensity ratio (%)					
		CZ	**CZN (A.C)**	**CZN (A.R)**	**ZC**	**ZCN (A.C)**	**ZCN (A.R)**
M-3d*	M^{3+} (Ce^{3+} or Zr^{3+})	7.0	7.1	9.1	21.6	23.4	44.0
Ni-2p	Ni metallic site (852.5eV)	-	-	12.2	-	-	40.8

* *(A.C) = after calcination*

* *(A.R) = after reduction*

* *M-3d is Ce-3d in Ce-rich catalyst & Zr-3d in Zr-rich catalyst*

3.2 Reaction test

3.2.1 Overview of ethanol steam reforming

The conversion of ethanol (X_{C2H5OH}), as well as the distribution of the products in terms of selectivity and hydrogen production rate at 550 and 750 over supports only and Ni, impregnated catalysts are reported in Table 4. It is well known that ethanol steam reforming is a reaction with a complex mechanism along several reaction pathways involving products such as CO, CO_2, CH_4, C_2H_4, CH_3CHO, CH_3COCH_3, and coke. The reaction pathways of major mechanisms in the literature are expressed by Equations 1 to 9 [12, 50-52]. However, in this study, which simplified the catalyst composition, the main products were simplified to CO, CO_2, CH_4, and C_2H_4 as summarized in Table 4, and carbon deposition hardly occurred. In addition, a simplified reaction pathway is shown in Fig. 3.9, and it also shows the reaction pathway (Fig. 3.9 – (A)) in which active oxygen participates and the generation pathway (Fig. 3.9 – (B)) of active oxygen.

Among them, the main reaction pathway of ESR included five reactions on three active sites in this study:

1) dehydration of ethanol at the metal cationic site on the support,

2) ethylene oxidation, water gas shift reaction, and water activation at the oxygen vacancy on the support, and

3) steam reforming of ethylene at the metallic Ni site.

First, Meijun Li et al. reported that Ethanol adsorbs and forms ethoxide, and then ethylene desorption results from a unimolecular E1 mechanism with concerted β–CH and C–O cleavage of the ethoxy. At higher temperature when the surface is covered with ethoxide, β-CH scission is activated and leaves labile O on the surface [53].

Second, for reactions related to oxygen vacancy, it has been widely accepted that catalysts with oxygen vacancy participate in reaction mainly through a Mars-van-Krevelen-like mechanism [37], in which reactant is oxidized by the O_x^- species generated over oxygen vacancy. The reductive reactant such as ethylene was molecularly or dissociatively adsorbed on the support or Ni metallic site. And the ethylene oxidized by the lattice oxygen to form either a selective oxidation product, such as CO, or complete oxidation products, such as CO_2, which were subsequently desorbed from the surface and

diffuse to the bulk fluid phase [54]. The oxygen vacancy sites were simultaneously replenished by the surface adsorption and dissociation of gaseous water molecules followed by the lattice O^{2-} diffusion [55]. Schematic of the mechanism by which oxygen vacancy participates over CZ, CZN, ZC, and ZCN catalysts, is summarized in Fig. 3.10.

(Reaction path)

Ethanol Dehydration

$C_2H_5OH(g) \rightarrow C_2H_4(g) + H_2O(g)$ $\Delta H_r^{o}{}_{298} = 45.5kJ/mol$ (1)

Water Gas Shift

$CO(g) + H_2O(g) \rightarrow CO_2(g) + H_2(g)$ $\Delta H_r^{o}{}_{298} = -41.2kJ/mol$ (2)

Ethylene Steam Reforming

$C_2H_4(g) + 2H_2O(g) \rightarrow 2CO(g) + 4H_2(g)$ $\Delta H_r^{o}{}_{298} = 210.1kJ/mol$ (3)

Ethanol Decomposition

$C_2H_5OH(g) \rightarrow CH_4(g) + CO(g) + H_2(g)$ $\Delta H_r^{o}{}_{,298} = 49.6kJ/mol$ (4)

Methane Steam Reforming

$CH_4(g) + 2H_2O(g) \rightarrow CO(g) + 3H_2(g)$ $\Delta H_r^{o}{}_{298} = 206.1kJ/mol$ (5)

Dehydrogenation

$C_2H_5OH(g) \rightarrow CH_3CHO(g) + H_2(g)$ $\Delta H_r^{o}{}_{298} = 68.9kJ/mol$ (6)

Acetone formation

$2CH_3CHO(g) \rightarrow CH_3COCH_3(g) + CO(g) + H_2(g)$ $\Delta H_r^{o}{}_{298} = 4.1kJ/mol$ (7)

Ethylene decomposition

$C_2H_4(g) \rightarrow 2C(s) + 2H_2(g)$ $\Delta H_r^{o}{}_{298} = -52.3kJ/mol$ (8)

Coke precursor oxidation

$C_xH_y + O_z \rightarrow C_{x-1}H_y + CO + O_{z-1}$ (9)

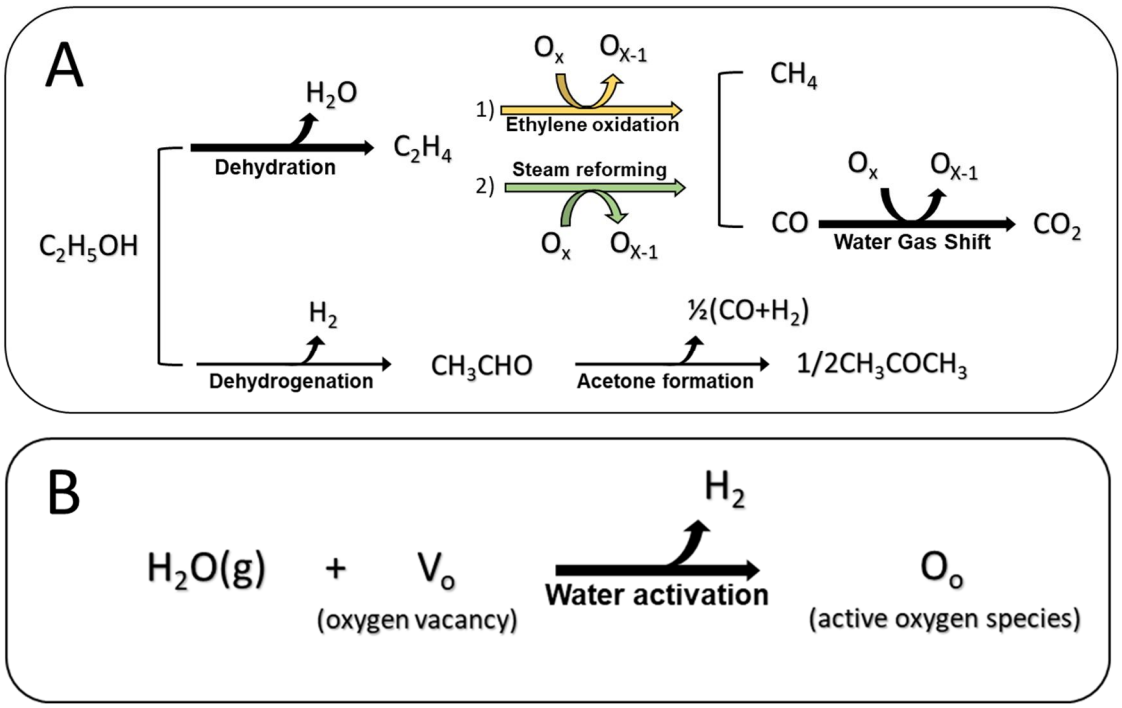

Figure 3.9. Reaction pathway of (A) ethanol steam reforming and (B) water split (water activation).

Table 4. Catalyst performance of the ESR reaction in 550 ℃ and 750 ℃ (reaction conditions: S/C = 3, GHSV = 10619 h^{-1}).

T ( )	Catalyst	$X_{ethanol}$ (%)	CO2/CO ratio	C- containing product selectivity (%)						H_2 selectivity (%)	H_2 Production rate [μmol/g•min]
				CO	CO_2	CH_4	C_2H_4	C_2H_6	CH_3COCH_3		
550	CZ	91.6	7.22	3.5	25.0	8.7	55.6	0.0	7.2	37.8	479.0
	ZC	90.2	No CO	0.0	10.3	2.7	84.3	0.0	2.7	15.7	171.9
750	CZ	100	2.20	15.6	34.5	32.0	13.8	1.4	2.7	43.3	788.5
	ZC	100	0.26	37.5	9.9	36.0	14.6	1.5	0.6	32.8	410.8
550	CZN	40.3	3.14	13.0	40.7	8.6	37.7	0.0	0.0	69.3	67.3
	ZCN	36.9	1.69	15.6	26.3	7.2	50.9	0.0	0.0	47.3	34.8
750	CZN	100	2.15	21.3	45.9	28.6	0.0	3.2	1.0	59.6	1112.2
	ZCN	100	0.29	56.0	16.7	26.4	0.1	0.7	0.0	57.0	829.2

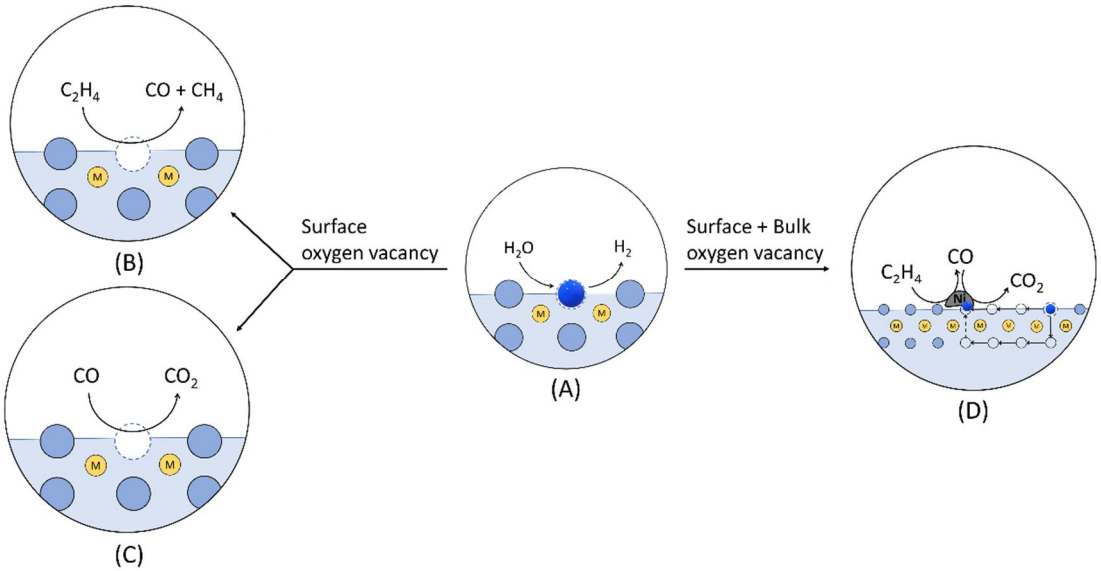

Figure 3.10. Schematic of the mechanism by which oxygen vacancy participates: (A) formation of active oxygen, (B) Ethylene oxidation, (C) Water gas shift reaction, and (D) Steam reforming on Ni metallic site.

3.2.2 Reaction results of support (CZ & ZC)

Product distributions as a function of TOS obtained for CZ and ZC catalysts during ethanol steam reforming at 550 and 750 are presented in Fig. 3.11.

Over CZ catalyst, ethanol conversion is 91.6% at 550 and reached 100% at 750 . At 550 , ethylene (C_2H_4) was the main reaction product (55.6% selectivity), whereas at 750 , when ethanol conversion was 100%, CO (15.6% selectivity), CO_2 (34.5% selectivity), and CH_4 (32% selectivity) were mainly detected. Accordingly, hydrogen was produced 479.0 μmol/g•min at 550 and it increased by 309.5 to become 788.5 μmol/g•min at the high conversions and temperatures.

Over ZC catalyst, ethanol conversion was 90.2% at 550 and reached 100% at 750 . At 550 , ethylene was the main reaction product (84.3% selectivity) even at the similar ethanol conversions to CZ with the less formation of CO, CO_2, and CH_4. Whereas at 750 , when ethanol conversion was 100%, CO (37.5% selectivity), CO_2 (9.9% selectivity), and CH_4 (36% selectivity) were mainly detected, and especially the CO_2 selectivity was very low compared to CO. Accordingly, hydrogen was produced 171.9 μmol/g•min at 550 and it increased by 238.9 to become 410.8 μmol/g•min at the high conversions and temperatures.

At 550 reaction result, both catalysts had similar ethanol conversions. The difference in conversion was only about 1% between CZ and ZC, and the product from the ethanol was mostly ethylene. Ethylene was a product of the dehydration reaction of ethanol. In addition, TGA results (Fig. 3.12) indicated the effect of carbon deposition in both catalysts was very small, so the amount of ethylene produced was similar in both catalysts. Therefore, the lower ethylene selectivity than ZC at CZ of 550 °C indicates that ethylene acts as a reactant to produce CO, CO_2, and CH_4. After conversion to ethylene, an oxygen-involved reaction occurred. Active oxygen was generated through a water activation reaction in which water was decomposed into hydrogen and active oxygen in oxygen vacancy. The generated active oxygen participated in ethylene oxidation and water gas shift reaction. The degree of ethylene oxidation can be determined by the selectivity of reacted ethylene. And the degree of water gas shift reaction can know how much CO was converted to CO_2 through the CO_2/CO ratio. Both reactions occurred in the same active site, oxygen vacancy. Therefore, a large amount of oxygen vacancy

produced a large number of active oxygen species and enhanced the ethylene oxidation and water gas shift reaction resulting higher hydrogen production of CZ. Through the reaction results, the role of oxygen vacancy was confirmed.

When the reaction temperature was raised to 750 , the reaction path was the same as the reaction result at 550 . However, a change in the selectivity of the reaction occurred. First, the selectivity of ethylene sharply decreases as the temperature increases. CZ showed a sharp decrease to 13.8% and ZC to 14.6%, respectively. The C-C bond of ethylene is easily broken as the temperature rises, which makes ethylene oxidation easier to occur and generates a greater amount of CO as a product. Second, when comparing the water gas shift reaction with respect to temperature through the CO_2/CO ratio, the CO_2/CO ratio decreases. The CO_2/CO ratio shows a sharp decrease from to 2.20 for CZ and 0.26 for ZC, respectively. The water gas shift reaction is an exothermic reaction and decreases with increasing temperature. Comparing the results of CZ and ZC, the selectivity of ethylene at 750 °C was similar, but the degree of water gas shift reaction in ZC shows a sharper decrease than in CZ. The lack of oxygen vacancy over ZC resulted in limited reaction routes for the active oxygen species that was temperature-dependent catalytic behavior.

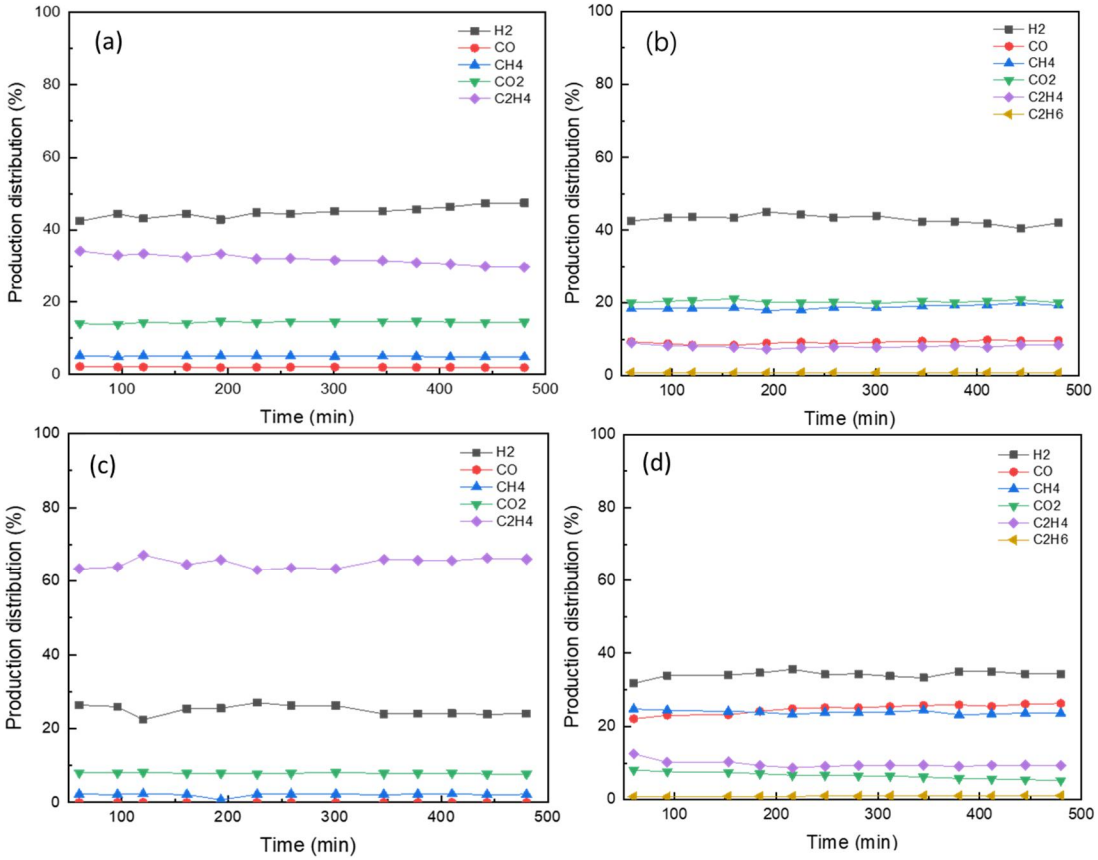

Figure 3.11. Product distributions versus TOS obtained during steam reforming for 8 hours over CZ ((a)550□, (b)750□) and ZC ((c) 550□, (d)750□).

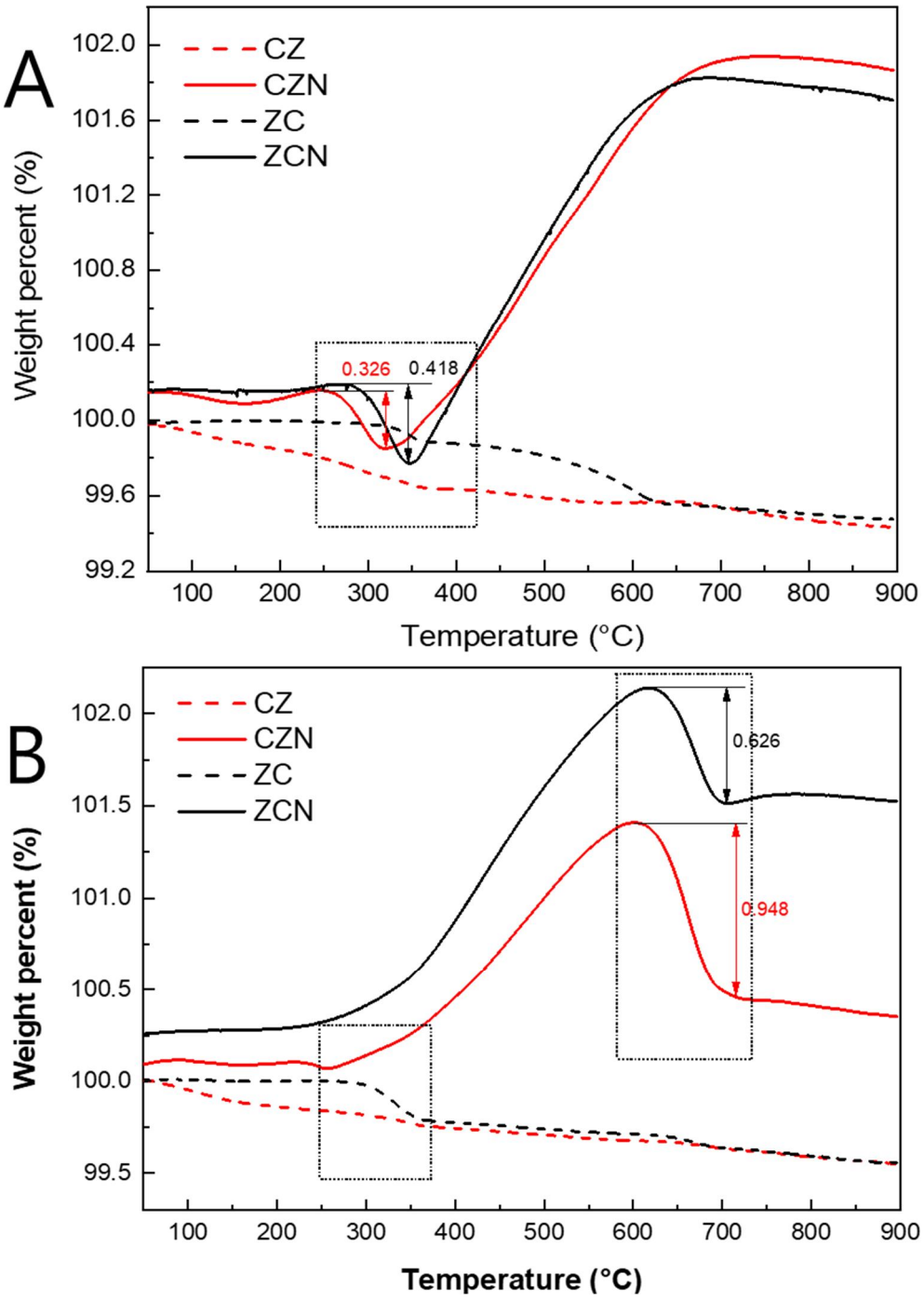

Figure 3.12. TGA results at (A) 550 ℃ and (B) 750 ℃ reactions

3.2.3 Reaction results of Ni-impregnated catalysts (CZN & ZCN)

Product distributions as a function of TOS obtained for CZN and ZCN catalyst during ethanol steam reforming at 550 and 750 are presented in Fig. 3.13.

Over CZN catalyst, ethanol conversion was a very low value of 40.3% at 550 and reached 100% at 750 . At 550 , ethylene (37.7% selectivity) and fully oxidized CO_2 (40.7% selectivity) were the main reaction product. At 750 , when ethanol conversion was 100%, all ethylene was converted as the reactant, and CO (21.3% selectivity), CO_2 (45.9% selectivity), and CH_4 (28.6% selectivity) were mainly detected. Accordingly, hydrogen was produced 67.3 μmol/g•min at 550 and it increases by 1044.9 to become 1112.2 μmol/g•min at high conversions and temperatures.

Over ZCN catalyst, ethanol conversion was also the very low value of 36.9% at 550 and reaches 100% at 750 . At 550 , ethylene (C_2H_4) was the main reaction product (55.6% selectivity), whereas, at 750 , when ethanol conversion is 100%, most of the ethylene was converted (0.1% selectivity) as reactant and CO (56.0% selectivity), CO_2 (16.7% selectivity), and CH_4 (26.4% selectivity) were mainly detected. Accordingly, hydrogen was produced 34.8 μmol/g•min at 550 and it increased by 794.4 to become 829.2 μmol/g•min at the high conversions and temperatures.

As Ni was impregnated, one more active site was added. Ni was the active point of steam reforming to cleavage the C-C bond, and the reaction proceeded with the participation of active oxygen through water activation. Through this reaction, the Ni active site helped in the conversion of ethylene. In addition, when Ni was impregnated, it affected the formation of the surface and the bulk oxygen vacancy as shown in Table 2.

In the 550 °C results, a notable result was the conversion of the Ni impregnated catalyst. In other studies, studying catalysts with high surface area, conversion increased as the amount of Ni increases. But in this study, the support had a very low surface area except for supports like Al_2O_3, and the excess Ni cluster peak at 855.5eV in Ni-2p XPS results shows an excess of Ni clusters was formed on the surface. Independent of the behavior of Ni metallic sites, the formation of Ni clusters can inhibit the reaction by blocking the access of reactants. This trend appeared in both CZN and ZCN catalysts, and the conversion decreased as Ni was impregnated from 92.18% to 47.48% for CZN and from 88.92% to 41.07% for ZCN with many fluctuations. In addition, the decrease in

ethanol conversion influenced the decrease in hydrogen production as shown in Table 4. However, when comparing selectivity, as Ni was impregnated on the support, the selectivity of C_2H_4 decreases, and the hydrogen selectivity increases. This indicated that Ni could act as an active site after ethanol was converted to C_2H_4. When the ethylene selectivity of CZN and ZCN was compared, it can be confirmed that CZN showed a lower value and was converted to CO, CO_2, and CH_4. It can be seen that the bulk oxygen vacancy affected the oxygen storage capacity and the amount of active oxygen as the surface oxygen vacancy.

When the reaction temperature was raised to 750 , ethanol was 100% converted. Since the ethanol-decomposed reaction was an endothermic reaction, conversion increased with temperature. In both catalysts, the selectivity of ethylene was reduced to near zero as almost all the ethylene was converted as a reactant. And the CO_2/CO ratio decreased from 3.14 to 2.15 for CZN and from 1.69 to 0.29 for ZCN. This was consistent with the results of support that the activation of ethylene oxidation and inhibition of the water gas shift reaction occurred at high temperatures. These results suggested that bulk oxygen vacancy contributes to OSC in the same way as surface oxygen vacancy did.

To elucidate another role of bulk oxygen vacancy, the selectivity ratio of CO_2 increased to C2 product (C_2H_4, C_2H_6) decreased when Ni was impregnated is summarized in Fig. 3.14 and table 6. This was to compare the degree of the active oxygen migration (Fig. 3.14 –(A)) when CO was generated from Ni for steam reforming (Fig. 3.14 –(B)) converting CO to CO_2 (Fig. 3.14 –(C)). This degree was explained through the ratio of the selectivity difference ($\Delta CO_2/\Delta C2$) before and after nickel loading. In addition, according to the H_2-TPR results, the bulk oxygen vacancy was more activated at high temperature, so the role of bulk oxygen vacancy was confirmed more clearly by comparing the low and high temperature results of CZN and ZCN. In the case of CZN, when the temperature increases from 550 to 750 , it increases from 0.88 to 0.95, whereas for ZCN, it decreases from 0.47 to 0.44. This result indicates that oxygen migration was activated in CZN where bulk oxygen vacancy exists, whereas oxygen migration did not occur in ZCN.

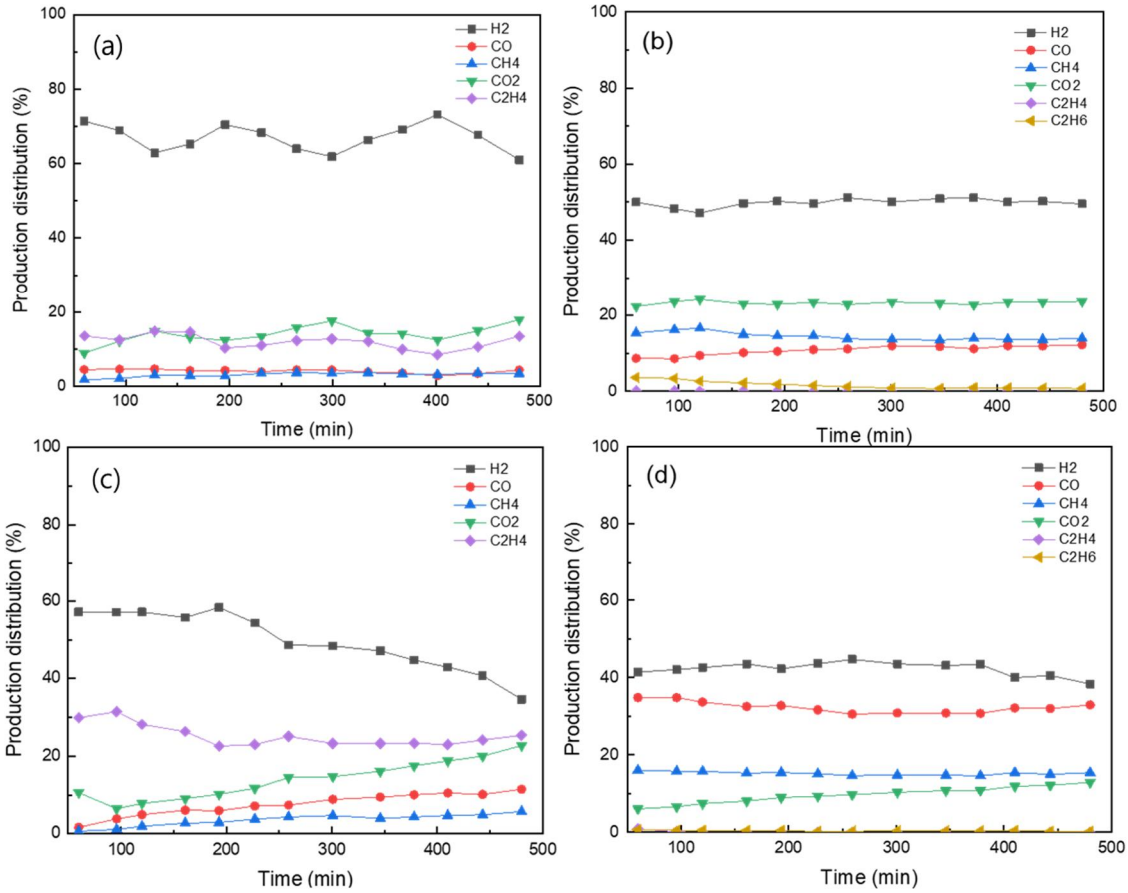

Figure 3.13. Product distributions versus TOS obtained during steam reforming for 8 hours over CZN ((a)550□, (b)750□) and ZCN ((c) 550□, (d)750□).

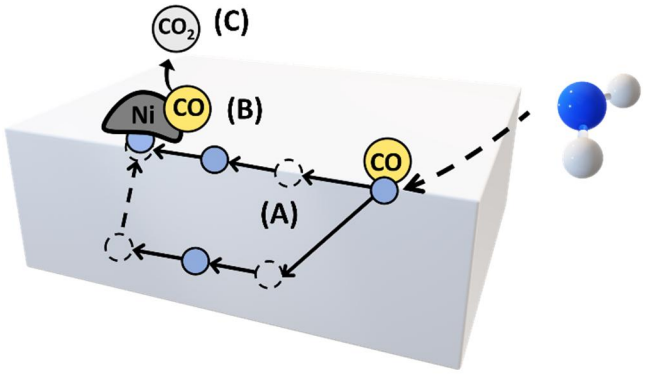

Figure 3.14. Schematic of (A) Oxygen migration, (B) CO formation on Ni, and (C) Conversion of CO to CO_2 on Ni.

Table 5. Migration rate of bulk oxygen species

Catalyst	$\Delta CO_2/\Delta C_2$ (550℃)	$\Delta CO_2/\Delta C_2$ (750℃)
CZN-CZ	**0.88**	**0.95**
ZCN-ZC	**0.47**	**0.44**

Chapter 4: Conclusions

In this work, the oxygen vacancy sites affecting hydrogen production over $Ni/Ce_xZr_{1-x}O_2$ were studied for ethanol steam reforming (ESR). To understand catalytic behavior depends on the lattice structures and temperatures over oxygen vacant sites, $Ce_xZr_{1-x}O_2$ as the support was modified with Ce-rich (CZ) and Zr-rich (ZC). From the results of characterization, it was revealed that oxygen vacancy was located on the surface and bulk, and there was a greater amount of oxygen vacancy in the CZ. Ni contributes to the activity of the surface oxygen vacancy of both CZ and ZC catalysts by helping the reduction of the support. The oxygen vacancy in the bulk ZC structure completely disappeared due to the Ni impregnation whereas the bulk oxygen vacancy of CZ was still maintained. Oxygen vacancy generated active oxygen species via the steam activation and then, the active oxygen species simultaneously involved steam reforming, water gas shift reaction, and ethylene oxidation during ESR. From the reaction result, the lack of oxygen vacancy over ZC resulted in limited reaction routes due to limited active oxygen species. The ZC catalyst, when compared with CZ, exhibited the limitation of the ethylene oxidation at 550 and water gas shift reaction at 750 , respectively. With the Ni species, even though the surface oxygen vacancy behavior over CZN and ZCN was the same, the oxygen-involved reaction and oxygen migration were enhanced with the bulk oxygen vacancy of CZN, resulting in the highest H_2 production of 1112.2 μmol/g•min for the CZN catalyst.

References

[1] M. Balat, Bioethanol as a Vehicular Fuel: A Critical Review, Energ Source Part A, 31 (2009) 1242-1255.

[2] G. Lazaroiu, D.-A. Ciupageanu, Multi-criteria decision making in sustainable renewable energy systems, International Multidisciplinary Scientific GeoConference: SGEM, 19 (2019) 325-332.

[3] Global CO emissions from land use change., 2021.

[4] R. Abro, X. Chen, K. Harijan, Z.A. Dhakan, M. Ammar, A comparative study of recycling of used engine oil using extraction by composite solvent, single solvent, and acid treatment methods, International Scholarly Research Notices, 2013 (2013).

[5] J.N. Armor, Catalysis and the hydrogen economy, Catalysis Letters, 101 (2005) 131-135.

[6] H. Balat, E. Kirtay, Hydrogen from biomass - Present scenario and future prospects, Int J Hydrogen Energ, 35 (2010) 7416-7426.

[7] I. Dincer, Green methods for hydrogen production, Int J Hydrogen Energ, 37 (2012) 1954-1971.

[8] M.J. Paredes, E. Moreno, A. Ramoscormenzana, J. Martinez, Characteristics of Soil after Pollution with Waste-Waters from Olive Oil Extraction Plants, Chemosphere, 16 (1987) 1557-1564.

[9] P. McKendry, Energy production from biomass (part 1): overview of biomass, Bioresource Technol, 83 (2002) 37-46.

[10] P. McKendry, Energy production from biomass (part 2): conversion technologies, Bioresource Technol, 83 (2002) 47-54.

[11] J.N. Armor, The multiple roles for catalysis in the production of H-2, Appl Catal a-Gen, 176 (1999) 159-176.

[12] A. Haryanto, S. Fernando, N. Murali, S. Adhikari, Current status of hydrogen production techniques by steam reforming of ethanol: A review, Energ Fuel, 19 (2005) 2098-2106.

[13] A.N. Fatsikostas, X.E. Verykios, Reaction network of steam reforming of ethanol over Ni-based catalysts, J Catal, 225 (2004) 439-452.

[14] G. Garbarino, A. Lagazzo, P. Riani, G. Busca, Steam reforming of ethanol-phenol mixture on Ni/Al2O3: Effect of Ni loading and sulphur deactivation, Appl Catal B-Environ, 129 (2013) 460-472.

[15] J. Contreras, J. Salmones, J. Colín-Luna, L. Nuño, B. Quintana, I. Córdova, B. Zeifert, C. Tapia, G. Fuentes, Catalysts for H2 production using the ethanol steam reforming (a

review), Int J Hydrogen Energ, 39 (2014) 18835-18853.

[16] N. Masiran, D.-V.N. Vo, M.A. Salam, B. Abdullah, Improvement on coke formation of CaO-Ni/Al2O3 catalysts in ethylene production via dehydration of ethanol, Procedia engineering, 148 (2016) 1289-1294.

[17] L. Zhang, J. Liu, W. Li, C. Guo, J. Zhang, Ethanol steam reforming over Ni-Cu/Al2O3-MyOz (M= Si, La, Mg, and Zn) catalysts, Journal of natural gas chemistry, 18 (2009) 55-65.

[18] C. Bernardo, I. Alstrup, J. Rostrup-Nielsen, Carbon deposition and methane steam reforming on silica-supported Ni Cu catalysts, J Catal, 96 (1985) 517-534.

[19] H. Wang, D.W. Blaylock, A.H. Dam, S.E. Liland, K.R. Rout, Y.-A. Zhu, W.H. Green, A. Holmen, D. Chen, Steam methane reforming on a Ni-based bimetallic catalyst: density functional theory and experimental studies of the catalytic consequence of surface alloying of Ni with Ag, Catal Sci Technol, 7 (2017) 1713-1725.

[20] G.Q. Yi, H.W. Yang, B.D. Li, H.Q. Lin, K. Tanaka, Y.Z. Yuan, Preferential CO oxidation in a H-2-rich gas by Au/CeO2 catalysts Nanoscale CeO2 shape effect and mechanism aspect, Catal Today, 157 (2010) 83-88.

[21] T. Montini, M. Melchionna, M. Monai, P. Fornasiero, Fundamentals and Catalytic Applications of CeO2-Based Materials, Chem Rev, 116 (2016) 5987-6041.

[22] M. Kuhn, S.R. Bishop, J.L.M. Rupp, H.L. Tuller, Structural characterization and oxygen nonstoichiometry of ceria-zirconia (Ce1-xZrxO2-delta) solid solutions, Acta Mater, 61 (2013) 4277-4288.

[23] K.C. Taylor, Nitric oxide catalysis in automotive exhaust systems, Catalysis Reviews—Science and Engineering, 35 (1993) 457-481.

[24] M. Ni, D.Y.C. Leung, M.K.H. Leung, A review on reforming bio-ethanol for hydrogen production, Int J Hydrogen Energ, 32 (2007) 3238-3247.

[25] E. Vesselli, G. Comelli, R. Rosei, S. Freni, F. Frusteri, S. Cavallaro, Ethanol auto-thermal reforming on rhodium catalysts and initial steps simulation on single crystals under UHV conditions, Appl Catal a-Gen, 281 (2005) 139-147.

[26] Y. Zhou, Y. Li, W.J. Shen, Shape Engineering of Oxide Nanoparticles for Heterogeneous Catalysis, Chem-Asian J, 11 (2016) 1470-1488.

[27] K. Wu, L.D. Sun, C.H. Yan, Recent Progress in Well-Controlled Synthesis of Ceria-Based Nanocatalysts towards Enhanced Catalytic Performance, Adv Energy Mater, 6 (2016).

[28] A. Trovarelli, J. Llorca, Ceria Catalysts at Nanoscale: How Do Crystal Shapes Shape Catalysis?, Acs Catal, 7 (2017) 4716-4735.

[29] M. Abu Shah, S. Md Nor, K.N. Ismail, A. Hadi, Study on the Structure and Morphology of CexZr (1-x) O2 Mixed Oxides, Advanced Materials Research, Trans Tech Publ, 2014, pp. 46-51.

[30] J. Chen, B.D. Carlson, T.J. Toops, Z. Li, M.J. Lance, S. Karakalos, J.-S. Choi, E. Kyriakidou, Methane combustion over Ni/CexZr1-xO2 catalysts: impact of ceria/zirconia ratio, ChemCatChem, 12 (2020).

[31] S. Rossignol, Y. Madier, D. Duprez, Preparation of zirconia–ceria materials by soft chemistry, Catal Today, 50 (1999) 261-270.

[32] C.Z. Yu, J. Fan, B.Z. Tian, D.Y. Zhao, G.D. Stucky, High-yield synthesis of periodic mesoporous silica rods and their replication to mesoporous carbon rods, Adv Mater, 14 (2002) 1742-+.

[33] H.D. Asfaw, M. Roberts, R. Younesi, K. Edstrom, Emulsion-templated bicontinuous carbon network electrodes for use in 3D microstructured batteries, J Mater Chem A, 1 (2013) 13750-13758.

[34] L.F. Liotta, G. Di Carlo, G. Pantaleo, G. Deganello, Co3O4/CeO2 andCo(3)O(4)/CeO2-ZrO2 composite catalysts for methane combustion: Correlation between morphology reduction properties and catalytic activity, Catal Commun, 6 (2005) 329-336.

[35] N. Guillen-Hurtado, A. Bueno-Lopez, A. Garcia-Garcia, Surface and structural characterisation of coprecipitated Ce (x) Zr1-x O-2 (0 a parts per thousand currency sign x a parts per thousand currency sign 1) mixed oxides, J Mater Sci, 47 (2012) 3204-3213.

[36] B. Sahoo, J. Joseph, A. Sharma, J. Paul, Surface modification of aluminium by graphene impregnation, Mater Design, 116 (2017) 51-64.

[37] P.M. Shah, J.W.H. Burnett, D.J. Morgan, T.E. Davies, S.H. Taylor, Ceria-Zirconia Mixed Metal Oxides Prepared via Mechanochemical Grinding of Carbonates for the Total Oxidation of Propane and Naphthalene, Catalysts, 9 (2019).

[38] L. Bai, F. Wyrwalski, C. Machut, P. Roussel, E. Monflier, A. Ponchel, Hydroxypropyl-beta-cyclodextrin as a versatile additive for the formation of metastable tetragonal zirconia exhibiting high thermal stability, Crystengcomm, 15 (2013) 2076-2083.

[39] W. Xiao, J.N. Wang, X.S. Zhao, J.W. Wang, G.J. Huang, L. Cheng, L.J. Jiang, L.G. Wang, Intrinsic defects and Na doping in Cu2ZnSnS4: A density-functional theory study, Sol Energy, 116 (2015) 125-132.

[40] S. Kouva, K. Honkala, L. Lefferts, J. Kanervo, Review: monoclinic zirconia, its surface sites and their interaction with carbon monoxide, Catal Sci Technol, 5 (2015) 3473-3490.

[41] L.V. Mattos, G. Jacobs, B.H. Davis, F.B. Noronha, Production of Hydrogen from Ethanol: Review of Reaction Mechanism and Catalyst Deactivation, Chem Rev, 112 (2012) 4094-4123.

[42] R. Bortamuly, G. Konwar, P.K. Boruah, M.R. Das, D. Mahanta, P. Saikia, CeO2-PANI-HCl and CeO2-PANI-PTSA composites: synthesis, characterization, and utilization as supercapacitor electrode materials, Ionics, 26 (2020) 5747-5756.

[43] M. Molinari, S.C. Parker, D.C. Sayle, M.S. Islam, Water Adsorption and Its Effect on the Stability of Low Index Stoichiometric and Reduced Surfaces of Ceria, J Phys Chem C, 116 (2012) 7073-7082.

[44] J.J. Pang, W.T. Li, Z.H. Cao, J.J. Xu, X. Li, X.K. Zhang, Mesoporous Cu2O-CeO2 composite nanospheres with enhanced catalytic activity for 4-nitrophenol reduction, Appl Surf Sci, 439 (2018) 420-429.

[45] F.C.F. Marcos, L.L. Lin, L.E. Betancourt, S.D. Senanayake, J.A. Rodriguez, J.M. Assaf, R. Giudici, E.M. Assaf, Insights into the methanol synthesis mechanism via CO2 hydrogenation over Cu-ZnO-ZrO2 catalysts: Effects of surfactant/Cu-Zn-Zr molar ratio, J Co2 Util, 41 (2020).

[46] H.D. Li, J. Ren, X. Qin, Z.F. Qin, J.Y. Lin, Z. Li, Ni/SBA-15 catalysts for CO methanation: effects of V, Ce, and Zr promoters, Rsc Adv, 5 (2015) 96504-96517.

[47] Y.S. Chen, J.F. Kang, B. Chen, B. Gao, L.F. Liu, X.Y. Liu, Y.Y. Wang, L. Wu, H.Y. Yu, J.Y. Wang, Q. Chen, E.G. Wang, Microscopic mechanism for unipolar resistive switching behaviour of nickel oxides, J Phys D Appl Phys, 45 (2012).

[48] D.H. Xiong, W. Li, L.F. Liu, Vertically Aligned Porous Nickel(II) Hydroxide Nanosheets Supported on Carbon Paper with Long-Term Oxygen Evolution Performance, Chem-Asian J, 12 (2017) 543-551.

[49] L.T. Do, E.W. Shin, Reinforcement of steam oxidative cracking of 1-methyl naphthalene by the synergistic combination of hydrogenation and oxidation over nickel-containing mixed oxide catalysts, J Catal, 371 (2019) 245-254.

[50] L. Maier, B. Schadel, K.H. Delgado, S. Tischer, O. Deutschmann, Steam Reforming of Methane Over Nickel: Development of a Multi-Step Surface Reaction Mechanism, Top Catal, 54 (2011) 845-858.

[51] S. Ogo, Y. Sekine, Recent progress in ethanol steam reforming using non-noble transition metal catalysts: A review, Fuel Process Technol, 199 (2020).

[52] A. Kumar, R. Singh, A.S.K. Sinha, Catalyst modification strategies to enhance the catalyst activity and stability during steam reforming of acetic acid for hydrogen production, Int J Hydrogen Energ, 44 (2019) 12983-13010.

[53] M.J. Li, Z.L. Wu, S.H. Overbury, Surface structure dependence of selective oxidation of ethanol on faceted CeO2 nanocrystals, J Catal, 306 (2013) 164-176.

[54] Z.Z. Pan, Y.D. Li, Y.C. Zhao, C.J. Zhang, H. Chen, Bulk phase charge transfer in focus-And in sequential along with surface steps, Catal Today, 364 (2021) 2-6.

[55] Z.L. Zhao, M. Uddi, N. Tsvetkov, B. Yildiz, A.F. Ghoniem, Redox Kinetics Study of Fuel Reduced Ceria for Chemical-Looping Water Splitting, J Phys Chem C, 120 (2016) 16271-16289.